Lithos 290–291 (2017) 136–158

Contents lists available at ScienceDirect

Lithos

journal homepage: www.elsevier.com/locate/lithos

Whole rock geochemistry, Zircon U–Pb and Hf isotope systematics of the Çangaldağ Pluton: Evidences for Middle Jurassic Continental Arc Magmatism in the Central Pontides, Turkey

Okay Çimen [a,b,*], M. Cemal Göncüoğlu [b], Antonio Simonetti [c], Kaan Sayit [b]

[a] Munzur University, Department of Geological Engineering, 62000 Tunceli, Turkey
[b] Middle East Technical University, Department of Geological Engineering, 06800 Ankara, Turkey
[c] University of Notre Dame, Department of Civil and Environmental Engineering and Earth Sciences, South Bend, Indiana 46556, USA

ARTICLE INFO

Article history:
Received 14 January 2017
Accepted 22 June 2017
Available online 28 June 2017

Keywords:
Çangaldağ Pluton
Central Pontides
Geochemistry
Geochronology
Intra-Pontide

ABSTRACT

The Central Pontides (Turkey) includes several igneous complexes, which are predominantly Permo-Carboniferous and Middle Jurassic in age. The Çangaldağ Pluton is one of the largest igneous bodies located in the northern Central Pontides, whose age and tectono-magmatic evaluation is important to constrain the geological evolution of the Northern Neotethys. The pluton tectonically overlies the Çangaldağ Metamorphic Complex, which represents an arc–back-arc complex of Middle Jurassic age. The Çangaldağ Pluton consists mainly of non-metamorphic gabbroic diorite, dacite porphyry, and lesser amount of granitic rocks. Geochemically, the various rock types are akin to volcanic arc magmas displaying Th/Nb and light rare earth element/heavy rare earth element enrichments. In-situ U–Pb age results of zircons from dacite porphyry and granite samples yield ages of 161 ± 5 Ma and 170 ± 2 Ma, respectively. Corresponding in-situ average $^{176}Hf/^{177}Hf$ initial ratios are 0.28287 ± 0.00004 and 0.28213 ± 0.00002 for the dacite porphyry and granite samples, respectively. These results are consistent with derivation from a subduction-modified mantle source. Based on Hf isotope compositions, T_{DM} model ages vary between 624 and 1512 Ma and suggest that the arc magmatism associated with the Çangaldağ Pluton may have involved partial melting of Neoproterozoic/Mesoproterozoic crustal rocks, a common feature in Gondwana-derived terranes. The geochemical, Hf isotope, and geochronological data reported here confirm the presence of a continental arc system during the Middle Jurassic in the Central Pontides, and suggests that the Çangaldağ Pluton formed during northward subduction of the Intra-Pontide branch of the Northern Neotethys.

1. Introduction

Turkey is part of the Alpine–Himalayan orogenic belt, which formed by the agglomeration of several terranes (Göncüoğlu, 2010; Okay and Tüysüz, 1999; Robertson et al., 2014), or continental micro-plates (Şengör and Yılmaz, 1981) during closure of different branches of the Tethyan Ocean. In NW Anatolia, the northernmost terrane consists of the Istanbul–Zonguldak Terrane (IZT), which represents the southern Eurasian margin. It is separated from the Sakarya Composite Terrane (SCT) to the south by the Intra-Pontide Suture Belt (IPSB; Göncüoğlu et al., 2000; Şengör and Yılmaz, 1981). In the south, the Izmir–Ankara–Erzincan Suture Belt (IAESB; Fig. 1A) marks the boundary between the SCT and the Anatolide–Tauride Terrane. All of these oceanic assemblages and continental fragments are related to the Tethyan evolution of Turkey during the Paleozoic and Mesozoic times.

The IZT displays a well-developed Paleozoic sequence from Early Ordovician to the Late Carboniferous (Chen et al., 2002; Dean et al., 1997; Özgül, 2012), which unconformably overlies the Neoproterozoic crystalline basement (Ustaömer et al., 2005). This crystalline basement is composed of remnants of an accreted intra-oceanic island arc, and oceanic crust that can be attributed to the Cadomian event (Göncüoğlu, 2010). Also, Permian granitoids locally cut these Paleozoic units (Okay et al., 2013; Şahin et al., 2009), and are unconformably overlain by Permo-Triassic red-beds and Middle Jurassic limestones (Okay et al., 2015). Lastly, all units are overlain unconformably by Upper Jurassic–Lower Cretaceous limestones and Lower Cretaceous turbidites (Uğuz and Sevin, 2007). There is an overall agreement that the IZT consists of Gondwana-derived terranes that were accreted to the southern margin of Eurasia at the end of Paleozoic, and remained there until the Late Mesozoic opening of the Black-sea.

In contrast, the SCT consists of Variscan and Cimmerian Terranes and their Alpine cover units (Göncüoğlu, 2010). The Variscan Terranes are composed of several metamorphic units; Söğüt Metamorphics (e.g. Göncüoğlu et al., 2000) in the west; Devrekani metamorphics in the

* Corresponding author at: Munzur University, Department of Geological Engineering, 62000 Tunceli, Turkey.
E-mail address: okaycimen@munzur.edu.tr (O. Çimen).

http://dx.doi.org/10.1016/j.lithos.2017.06.020
0024-4937/

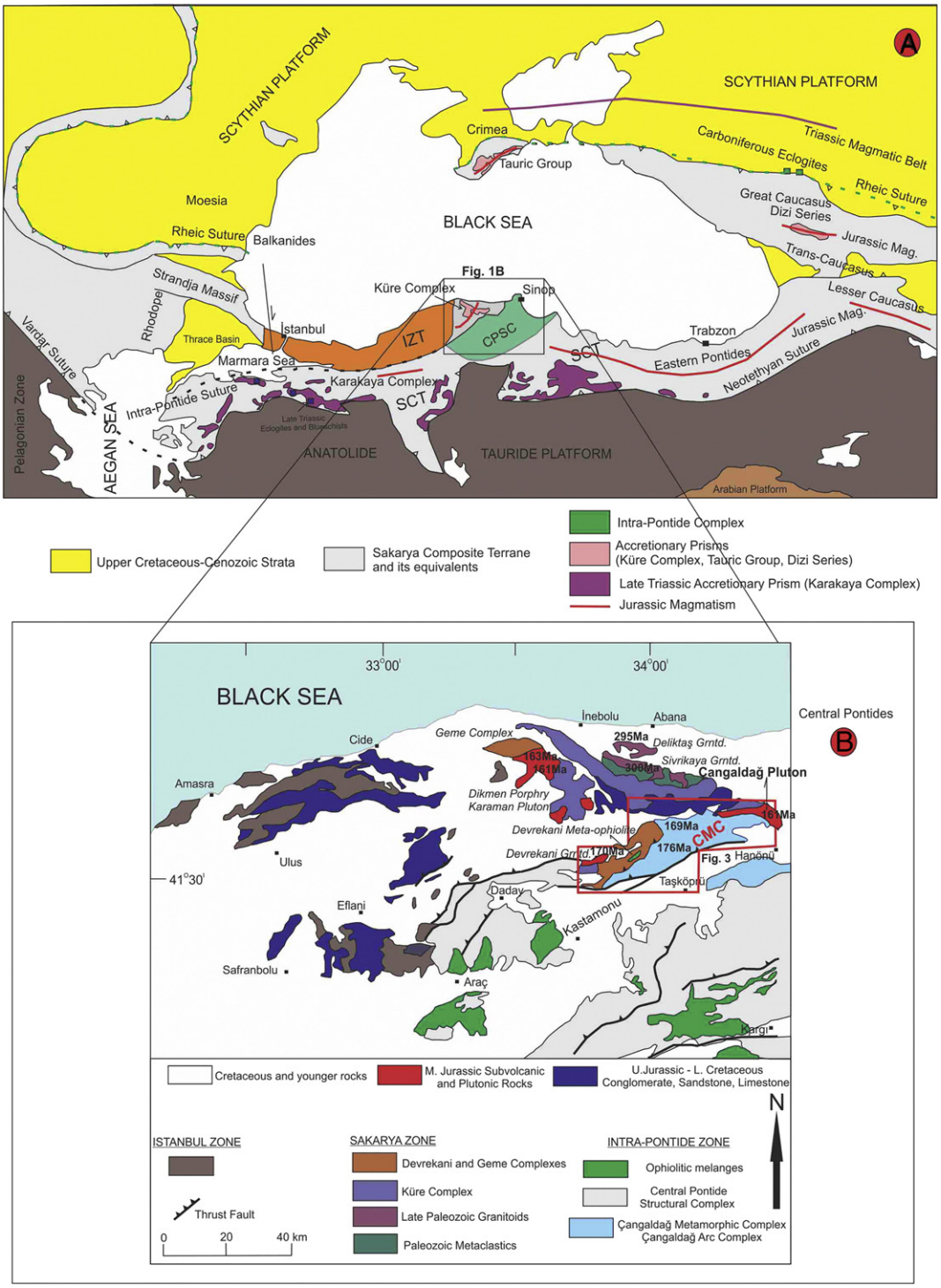

Fig. 1. (A) Tectonic map of the Black Sea region; CPSC: Central Pontide Structural Complex. SCT: Sakarya Composite Terrane. IZT: İstanbul–Zonguldak Terrane. (B) The main structural units of the Central Pontides. CMC: Çangaldağ Metamorphic Complex. Grntd: Granitoid. Age data taken from Nzegge (2008), Okay et al. (2014), Çimen (2016) and this study. (Panel A: modified from Okay and Nikishin, 2015; Panel B: modified after Göncüoğlu et al., 2012, 2014; Okay et al., 2015; Ustaömer and Robertson, 1999.)

Central Pontides and Pulur metamorphics (e.g. Topuz et al., 2004) in the east, which mainly include ortho/paragneiss, amphibolite and marble (Göncüoğlu, 2010; Okay et al., 2006). The Cimmerian units in SCT are mainly represented by the "Karakaya Complex (e.g. Okay and Göncüoğlu, 2004) that include mainly crustal rocks (e.g. Sayit and Göncüoğlu, 2009), and subduction–accretion prism material of the Triassic Cimmerian Ocean. The Jurassic–Cretaceous cover of the SCT represents a platform margin.

The geological interpretation of the intervening Intra-Pontide Suture stretching from NW Biga Peninsula to eastern Central Pontides, however, remains a matter of debate. In particular, there are several tectonic models that have been proposed. The first hypothesis suggests a multiple branch model for the Neotethyan Ocean during the Mesozoic time and advocates the existence of the IPO (Akbayram et al., 2013, 2016; Çimen et al., 2016; Göncüoğlu et al., 2008, 2012, 2014; Marroni et al., 2014; Okay et al., 2006; Robertson and Ustaömer, 2004; Sayit

et al., 2016; Şengör and Yılmaz, 1981), especially in NW Anatolia. Here, there are different ideas in relation to the time of opening and closure of the IPO. The second model suggests that these ophiolitic mélanges belong to the Izmir–Ankara–Erzincan branch of the Neotethyan Ocean (single-strand model) and strike-slip faulting that occurred during the Late Cretaceous time; this caused displacement of the Izmir–Ankara–Erzincan oceanic units to their present locations (Elmas and Yiğitbaş, 2001). The third view suggests that the Intra-Pontide Suture (IPS) represents the continuation of the Rheic Ocean in Turkey (Okay et al., 2008; Stampfli and Borel, 2002), or remnants of the Paleotethys ocean (Bozkurt et al., 2013; Yılmaz et al., 1997).

In the Central Pontides (Fig. 1), the IZ, the SCT and members of the Intra-Pontide Suture belt are juxtaposed either by thrusts or by branches of the North Anatolian Transform Fault. Here, the Intra-Pontide Suture is represented by the Central Pontide Structural Complex (CPSC; Fig. 1B; Tekin et al., 2012) comprising the remnants of the Intra-Pontide Ocean (IPO; e.g. Çimen, 2016; Göncüoğlu et al., 2012, 2014; Sayit et al., 2016). From N to the S it comprises slices of the Çangaldağ Metamorphic Complex, the Emirköy, Daday, Domuz Dağ metamorphic units, Ayli Dağ Ophiolite, and the Arkot Dağ Mélange (e.g. Frassi et al., 2017).

These main tectonic units have been investigated by numerous researchers (e.g. Aydın et al., 1995; Aygül et al., 2016; Çimen et al., 2016; Göncüoğlu et al., 2012, 2014; Günay et al., 2016; Marroni et al., 2014; Okay and Nikishin, 2015; Okay et al., 2013, 2014, 2015; Sayit et al., 2016; Tüysüz, 1990; Ustaömer and Robertson, 1999). However, there is a lack of consensus in relation to the origin and tectonic evolution of the CPSC. In particular, conflicting views remain in the relations, paleogeographic and tectonic settings and ages of these tectonic units.

Using a multidisciplinary approach, we focused on evaluation of the tectono-magmatic features and ages of especially magmatic complexes in the northern Central Pontides. Overall, the northern Central Pontides includes several igneous complexes (Fig. 1B), which are predominantly Permo-Carboniferous (Deliktaş and Sivrikaya) and Middle Jurassic (e.g. Devrekani) in age (Boztuğ and Yılmaz, 1995; Nzegge, 2008; Okay et al., 2014). These complexes were first recognized as the Kastamonu Granitoid Belt (KGB; Yılmaz and Boztuğ, 1986), and interpreted as the magmatic products of orogenic collisional tectonics and crustal thickening during northward subduction of the Paleotethyan Ocean, or southward subduction of the Küre marginal basin (e.g. Boztuğ et al., 1995; Kozur et al., 2000; Nzegge, 2008; Ustaömer and Robertson, 1999; Yılmaz and Boztuğ, 1986). The Çangaldağ Pluton (CP; Çimen, 2016) is the largest (~20 km long and ~5 km wide) igneous body in the Central Pontides. It is located geographically between the subunits of the SCT and the CPSC. Despite its location within a tectonically important area in the northern CPSC, there are no published geochemical and radiometric age data for this pluton. Therefore, petrological, geochemical, and geochronological studies are needed and critical for better understanding the paleo-tectonic setting and geological evolution of the Central Pontides. Hence, this study reports the first geochemical, zircon U–Pb and Hf isotope data from the Çangaldağ Pluton in order to evaluate its tectono-magmatic evolution, and provide useful insights for the Mesozoic geodynamic evolution of the northern margin of the IPO.

2. Geological framework

Within the Central Pontides from the northwest to southeast (Fig. 2), there are several important tectonic units such as the Küre Complex, Geme Complex, Devrekani Metamorphics, Çangaldağ Metamorphic Complex (CMC), and the oceanic metabasalt–metaturbidite members, ophiolites and ophiolitic melanges of the CPSC (e.g. Aygül et al., 2016; Çimen, 2016; Göncüoğlu et al., 2012, 2014; Okay et al., 2006, 2013, 2014; Ustaömer and Robertson, 1999), which are described successively below.

2.1. Küre Complex

The Küre Complex is a dismembered ophiolite bearing thrust-imbricated deep-sea sediments (Ustaömer and Robertson, 1999). The ophiolitic rocks include serpentinized harzburgite, massive gabbro, sheeted dykes and basic volcanics. According to Kozur et al. (2000), this complex consists of three main tectonostratigraphic units, which are Küre Ridge Unit (low grade metamorphics, a Lower and Middle Triassic shallow marine sequence), Küre Ocean Unit (siliciclastic turbidites and olistostromes, Middle Jurassic molasse type shallow-marine sandstone, siltstone and shale, overlying a thick oceanic basalt and the upper part of an ophiolite), and Çalca Unit (Pelsonian to upper Norian Hallstat Limestone and Lower Jurassic deep-marine shale and marl). Its affiliation to one of the main terranes is disputed. The conflicting ideas range from supra-subduction-type oceanic crust of the Cimmerian Ocean (i.e., equivalent of the Karakaya Complex of SCT) to representative of Meliata–Maliac–Pindos oceanic system or a single marginal basin (Küre Ocean; for a detailed discussion and references see Ustaömer and Robertson, 1999).

2.2. Geme Complex

A significant amount of geological and geochronological data in relation to the Geme Complex has been recently reported by Okay et al. (2014). The complex consists mainly of gneiss and migmatite with minor amphibolite, marble and cross-cutting granitic veins and stocks, and is intruded by the Middle Jurassic (Fig. 1B; 163 Ma) Dikmen Porphyry. This crystalline basement is overlain disconformably by Lower Cretaceous sandstone and shale. These field relations indicate a

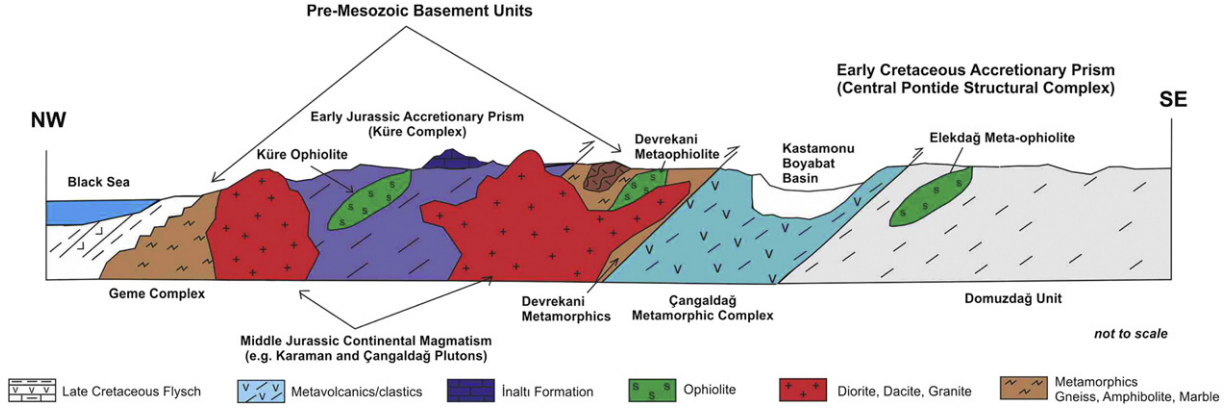

Fig. 2. Simplified cross section of the Central Pontides.
(Modified from Çimen, 2016; Ustaömer and Robertson, 1999.)

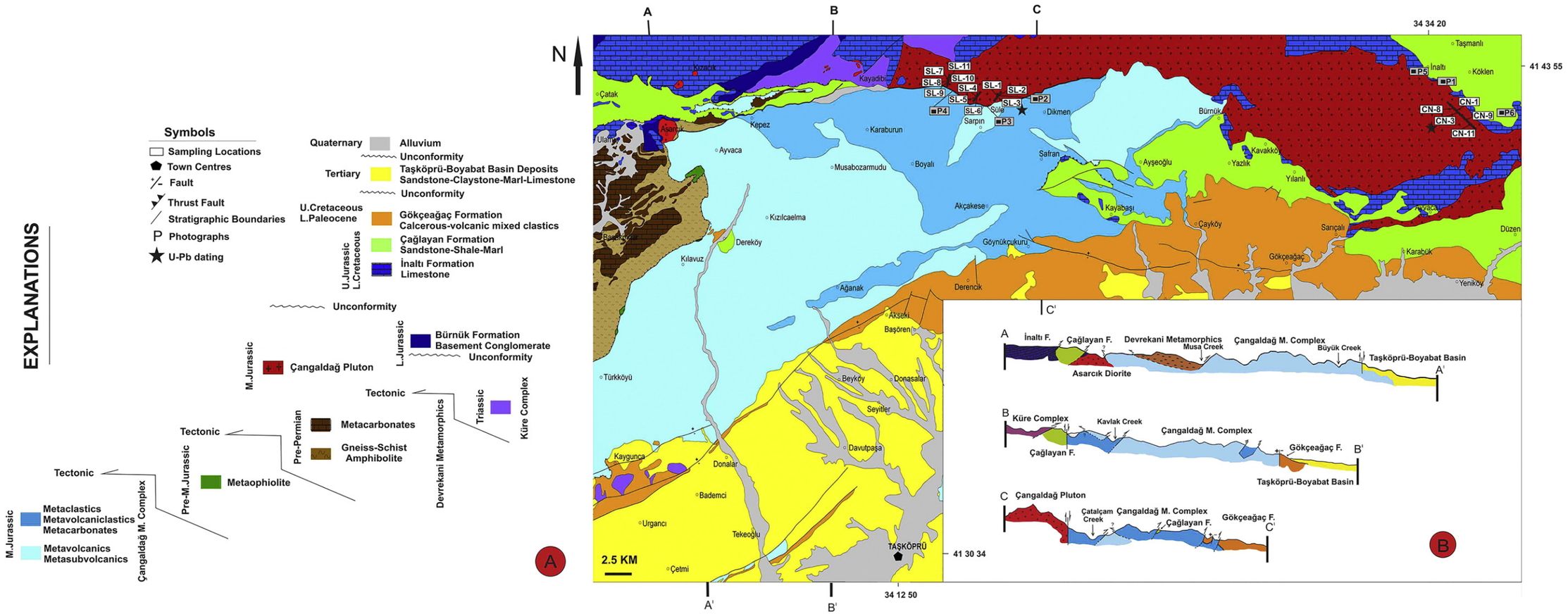

Fig. 3. (A) Geological map of the study area. (B) Cross sections from the North to South. (Modified from Konya et al., 1988.)

pre-Callovian metamorphic age for the Geme Complex. This unit is interpreted as remobilized Late Neoproterozoic and Hercynian basement of the Central Pontides (Okay et al., 2014).

2.3. Devrekani Metamorphics

This unit is located between the Küre and Çangaldağ Metamorphic Complexes (Fig. 1B). Similar to the Geme Complex, it is generally composed of gneiss, amphibolite, and meta-carbonate, which were metamorphosed in amphibolite and granulite facies conditions (e.g. Boztuğ et al., 1995). Middle and Late Jurassic ages (170 Ma to 149 Ma) were previously assigned for metamorphism by Yılmaz and Bonhomme (1991) based on K–Ar mica and amphibole dates. Recently, Okay et al. (2014) and Gücer et al. (2016) have also reported Jurassic metamorphic ages (150 Ma and 156 Ma). Gücer et al. (2016) suggested that the protoliths of the amphibolites, orthogneisses, and paragneisses are island-arc tholeiitic basalts, I-type calc-alkaline volcanic arc granitoids, and clastic sediments (shale-wackestone), respectively. U–Pb date of 264 Ma ± 90 (lower intercept age) for an orthogneiss, which cuts the Devrekani Metamorphics indicates a pre-Permian age for this unit (Çimen, 2016). In brief, the Devrekani metamorphic rocks may represent a crystalline basement of unknown age, intruded by a Permo-Carboniferous arc and overprinted by Jurassic metamorphism. Terranes with similar geological features and ages are reported from the basement of the SCT (e.g. Göncüoğlu et al., 2000) and the Eastern Pontides (e.g. Karslı et al., 2017). The contact of the Devrekani Metamorphics with the structure underlying the CMC is a compressional oblique fault.

2.4. Çangaldağ Metamorphic Complex (CMC)

The CMC is the northernmost unit of the CPSC; it was first described as a metaophiolite body (Boztuğ and Yılmaz, 1995; Tüysüz, 1990; Yılmaz, 1983). Later, Ustaömer and Robertson (1999) described it as a structurally thickened pile of mainly volcanic rocks and subordinate volcaniclastic sedimentary rocks, which overlie a basement of sheeted dykes in the north and basic extrusives in the south. It has also been defined as a pre-Jurassic metabasite–phyllite–marble unit (Okay et al., 2006). A single U–Pb zircon age of 169 ± 2 Ma from a metadacite sample (Okay et al., 2014), which represents the protolith of the CMC, indicates the Middle Jurassic magmatism. This U–Pb age, combined with the geochemical data from Ustaömer and Robertson (1999) was used by Okay et al. (2013, 2014) to assign the CMC to a Middle Jurassic arc. Previously, Middle Jurassic (153 Ma) and Early Cretaceous (126 and 110 Ma) K–Ar metamorphic ages for metabasic rocks and phyllites, respectively, were reported by Yılmaz and Bonhomme (1991). Recently, Okay et al. (2013) proposed an Early Cretaceous metamorphic age (between 136 and 125 Ma) for this complex based upon Ar–Ar mica dating of phyllites. Lastly, Çimen (2016) has obtained a Middle Jurassic intrusion age for the magmatism on the basis of detailed zircon U–Pb data from metarhyodacites. Geochemically, Çimen et al. (2016) put forward that the CMC was formed in an arc basin system within the Intra-Pontide Ocean during Middle Jurassic time, and was subsequently metamorphosed during the Early Cretaceous closure of this ocean.

2.5. Southern tectono-metamorphic members of the CPSC

To the south of the Kastamonu-Boyabat Tertiary basin (Figs. 2 and 3), the >5000 m-thick main body of the CPSC crops out. It comprises several tectono-metamorphic units with variably metamorphosed metabasalts and turbidites with rare carbonate rocks, ophiolitic mélanges and more or less complete slivers/slide-blocks of ophiolites (Frassi et al., 2016; Göncüoğlu et al., 2012, 2014; Marroni et al., 2014; Okay et al., 2006, 2013; Ustaömer and Robertson, 1999). A number of different names were used for these slices, which are correlated by Frassi et al. (2017).

Geochemically, the metabasic rocks are characterizing members of an arc–back arc system (Sayit et al., 2016) of unknown age, whereas the ophiolites represent a supra-subduction-type oceanic lithosphere of Middle Jurassic age (Göncüoğlu et al., 2012). In contrast, the blocks of radiolarian cherts associated with basalts within the mélange wedges yielded a wide range of ages between Late Triassic (Tekin et al., 2012) and Early Cretaceous (Göncüoglu et al., 2015). The metamorphism and deformation in all different tectonic units is polyphase and includes an earlier phase of amphibolite facies (Marroni et al., 2014) followed by a high pressure–low temperature (HP–LT) metamorphic phase that attains eclogite facies conditions (e.g. Okay et al., 2006). The overprinting phases mainly represent high pressure greenschist and greenschist facies conditions (Aygül et al., 2016; Frassi et al., 2016, 2017). The HP–LT metamorphic Ar–Ar ages of this unit have been determined as Late Jurassic (160–170 Ma) and Early Cretaceous (105 Ma) (Aygül et al., 2016; Frassi et al., 2017; Okay et al., 2006). The exhumation age of the HP–LT metabasic rocks to shallower structural levels is dated as Early Paleocene by apatite fission-track method (Frassi et al., 2017). Overall, the characteristics of the southern tectono-metamorphic members of the CPSC are interpreted to represent a subduction-related tectonic mélange (Frassi et al., 2016, 2017; Okay et al., 2006, 2013; Sayit et al., 2016) within the Intra-Pontide Subduction–Accretion Complex.

2.6. Cover units

The oldest cover sediments overlying the Çangaldağ Pluton and the surrounding tectonic units (e.g., CMC, Devrekani and Küre Complexes) are the Kimmeridgian to Berriasian İnaltı, Barremian to Albian Çağlayan (Aydın et al., 1995; Kaya and Altıner, 2014; Okay et al., 2006), and Upper Cretaceous Gökçeağaç formations, respectively. The Tertiary Taşköprü-Boyabat Basin units unconformably overlie the CPSC.

The İnaltı formation outcrops mainly in the north of the Çangaldağ area. It overlies the Küre Complex, CP, and CMC (Fig. 3B). This unit is unconformably overlain by the Early Cretaceous Çağlayan formation. The latter was first recognized by Ketin and Gümüş (1963). It is ~395 m thick and its origin attributed to shallow marine and reef/fore-reef carbonate platform (Kaya and Altıner, 2014). In the field they occur as white and gray recrystallized limestones (Fig. 4E).

The Çağlayan formation consists predominantly of alternating beds of sandstone and shale (Fig. 4F), and unconformably overlies the CMC in the south. The sandstone beds are gray-to-yellowish and their thicknesses range from thin (~5 cm) to thick (~60 cm). The shale beds are mostly thinner and gray in color. Şen (2013) proposed that the maximum thickness of this unit is ~3000 m. The Çağlayan formation displays typically turbiditic character, and includes well-developed sedimentary structures graded bedding, flute casts, grooves, and slump structures (Okay et al., 2013). This unit is unconformably overlain by Upper Cretaceous pelagic limestones (Okay et al., 2006, 2013).

The Gökçeağaç formation, which was previously named as the Yemişliçay Formation by Ketin and Gümüş (1963), mainly includes tuff material with volcanic fragments, generally andesitic and basaltic in nature, which have a matrix with calcareous clastics. Generally, it disconformably overlies the CMC in the south of the study area (Fig. 3).

The NE–SW trending Boyabat-Taşköprü Basin is filled predominantly by Tertiary conglomerate, sandstone, sandy limestone, and limestone (Uğuz and Sevin, 2007; Fig. 3). This basin is delineated by the Ekinveren fault in the north. In the southern part of the study area, the Tertiary units unconformably overlie the CMC and the remaining older units (Fig. 3).

3. Çangaldağ Pluton (CP)

3.1. Geological features

The CP outcrops as an NE–SW elongate plutonic body (Fig. 3) in the north of CMC. The CP is composed of granite, gabbroic diorite, and dacite

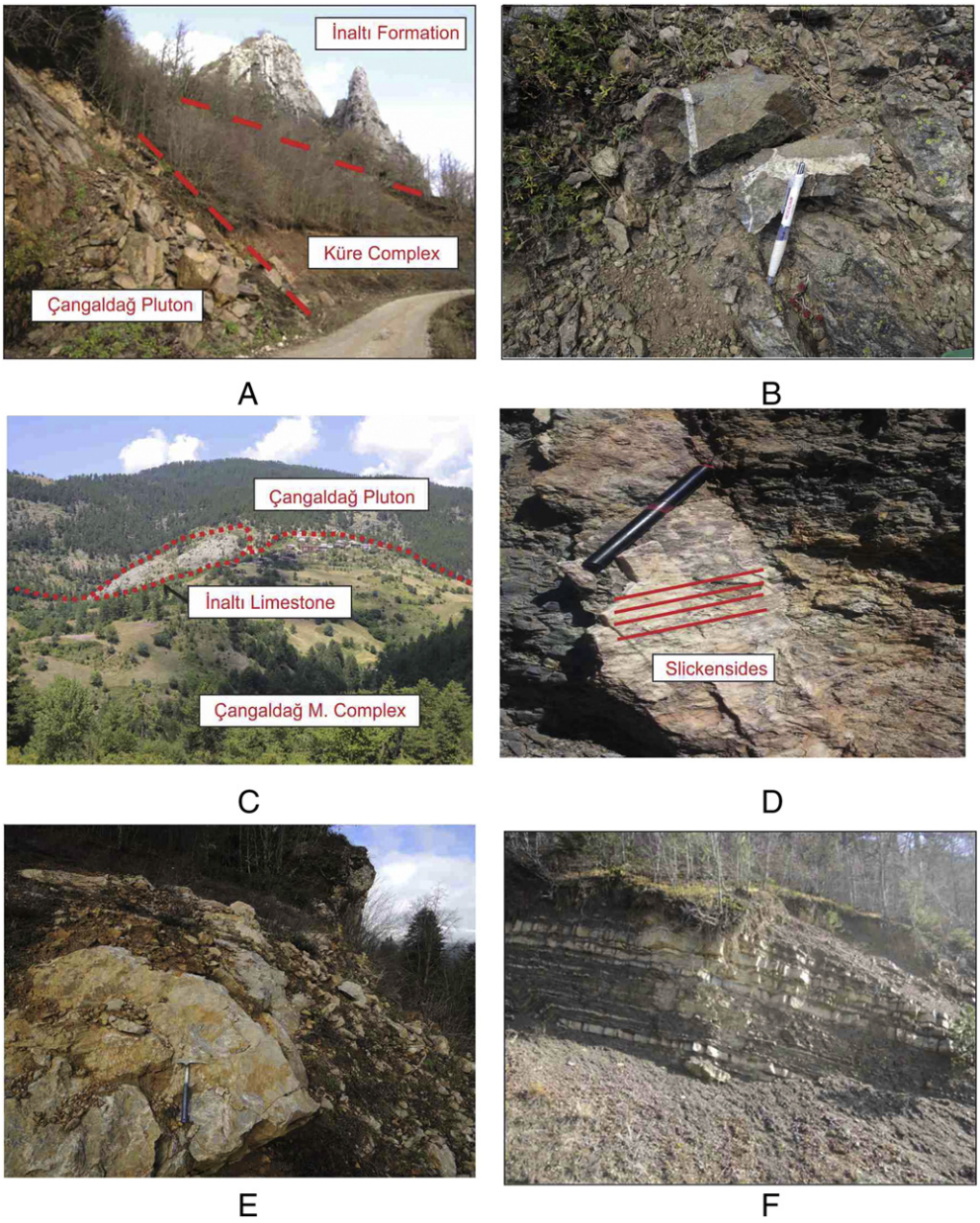

Fig. 4. (A) Field relations between the Çangaldağ Pluton, Küre Complex, and Inaltı formation (Locality P1). (B) The cross-cutting relation between granite veins and dioritic rocks within the Çangaldağ Pluton (Locality P2). (C) The strike-slip bounding with a sliver of İnaltı Limestone at the contact (Locality P3). (D) An image illustrating slickensides (strike-slip fault) (Locality P4). (G) A close-up image of the İnaltı formation (Locality P5). (H) Image illustrating the Çağlayan formation with alternating sandstone and shale units (Locality P6).

porphyry. Previous studies have argued that this large intrusive body cuts the CMC (Aydın et al., 1995; Yılmaz and Boztuğ, 1986) in the south and the Triassic Küre Complex in the east. It is overlain by the Upper Jurassic İnaltı Formation in several locations. Based on field observations, this contact is tectonic in nature and represents a regional scale strike-slip fault and not an intrusive relationship (Fig. 4C, D). However, intrusive contacts between the CP and the Küre Complex as well as Devrekani Metamorphics have been observed in this study. Primary depositional contacts between the İnaltı formation and the CP were observed in the mapped area (Fig. 4A).

The main body of the pluton is composed of gabbroic diorite all along the E–W trending Çangaldağ ridge. The dacite porphyries occur predominantly in the east, and may represent the marginal facies of this large dioritic body, reflecting the zoned character of this igneous body with a mafic core surrounded by a more felsic rim. The mineralogical composition of some diorites can be observed at hand specimen scale, and consists mainly of plagioclase and amphibole. In contrast, alkali feldspar phenocrysts can be identified by naked eye in the dacite porphyry samples. Additionally, the dioritic rocks are intruded by granitic veins (Fig. 4B) that occur predominantly in the western part of the pluton (to the north of Süle village, Fig. 3). This observation suggests that the felsic phases formed after diorite emplacement, a feature that is corroborated by the presence of mafic enclaves within the former. All rock types within the CP are devoid of metamorphic features.

3.2. Petrography

The primary igneous minerals of the gabbroic diorites are plagioclase, amphibole, and clinopyroxene (Fig. 5A), and define a holocrystalline/porphyritic texture. Hornblende is among the common phases in the diorites, and it exhibits greenish-to-brownish colors

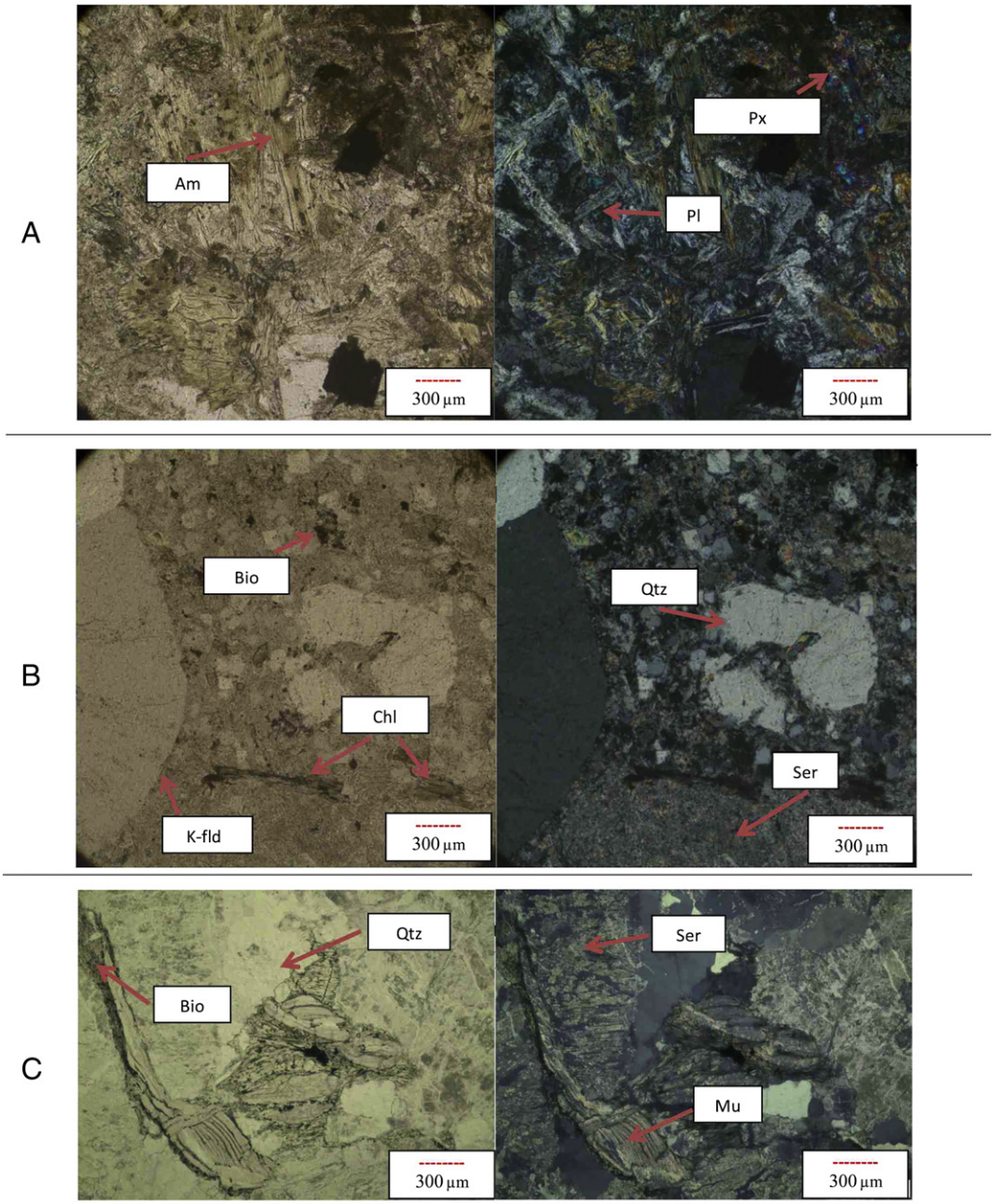

Fig. 5. Thin section images of: (A) mineral assemblages within gabbroic diorites, (B) mineral assemblage within dacite porphyries, (C) mineral assemblages associated with granites (all images 4×, PPL: plane polarized light, XPL: cross polarized light). Abbreviations: Am: amphibole, Px: pyroxene, Pl: plagioclase, Bio: biotite, Chl: chloritization, K-Fld: K-feldspar, Qtz: quartz, Ser: sericitization, Mu: muscovite.

with subhedral to euhedral crystals. It is commonly altered to chlorite minerals. The other predominant phase is plagioclase, which is characterized mainly by subhedral grains. Alteration of the plagioclase is frequently observed. Clinopyroxene is typically subhedral to euhedral in form and marginally replaced by chlorite.

The dacite porphyries also exhibit porphyritic texture, and the phenocryst phases are K-feldspar, plagioclase, quartz and biotite that are hosted within a fine-grained groundmass (Fig. 5B). The quartz crystals have anhedral and subhedral shapes. In some samples, corroded quartz crystals (Fig. 5B) suggest that interaction between these minerals and melt took place during their crystallization. The second common mineral is K-feldspar and it is mostly altered to the sericite. Plagioclases have also been partly replaced by calcite. Additionally, some biotite crystals have been slightly altered to chlorite minerals. Evidences for alteration include sericitization of K-feldspar along with chloritization of biotite in some samples.

The granite samples are mainly composed of K-feldspar, plagioclase, quartz, biotite, hornblende and muscovite, and display holocrystalline and porphyritic texture (Fig. 5C). The K-feldspar crystals are partly altered, and occur mainly as anhedral and subhedral crystals. The plagioclase minerals display polysynthetic twinning and have mainly subhedral shapes. Some sericite alteration is observed within K-feldspar and plagioclase grains. Quartz crystals display typical wavy extinction, and some quartz veins are found within these samples. Hornblende crystals show greenish to brownish colors with subhedral to euhedral shapes. Evidences of deformation and metamorphism are confined to mylonitic zones, which are also characterized by intensive alteration and mineralization.

4. Analytical methods

4.1. Whole rock geochemistry

A total of sixteen rock samples were selected for geochemistry. Major and trace element abundances were determined by ICP-OES (Inductively Coupled Plasma Optical Emission Spectrometry) and ICP-MS (Inductively Coupled Plasma Mass Spectrometry), respectively, at Acme Analytical Laboratories (Canada), following a lithium metaborate/tetraborate fusion and dilute nitric digestion. Loss on ignition (LOI) was determined based on weight difference after ignition at 1000 °C. Also, several duplicate analyses of samples were conducted in order to evaluate the procedural duplication and standard deviation of the results reported here. The geochemical classification diagrams were prepared using Geochemical Data Toolkit (GCDkit) software (Janoušek et al., 2006).

4.2. U–Pb geochronology

Two samples (dacite porphyry and granite) from CP were investigated for geochronological purposes. Subsequent the sample preparation process that included heavy mineral separation and careful hand-picking of crystals with the use of a petrographic microscope, ~50 zircon grains were embedded on glass slides and polished to expose their internal structure. Prior to Laser Ablation (LA)-Multicollector-(MC)-ICP-MS analysis, the zircons were then imaged by cathodoluminesence using a Cameca SX50 electron microprobe instrument (Figs. 6 and 7). Three well established and recognized zircon standards, Plešovice (Slama et al., 2008), 91500 (Wiedenbeck et al., 1995), and GJ-1 (Jackson et al., 2004) were analyzed throughout the analytical sessions in order to validate and ensure the accuracy of the in-situ U–Pb geochronological results reported here (Tables 2 and 3).

LA-MC-ICP-MS instrument configuration consists of a NuPlasmaII MC-ICP-MS instrument (Nu Instruments, UK) coupled to a NWR193 nm excimer laser ablation system (ESI-NWR). The mounts containing zircon samples and standards (Plešovice, 91500, GJ-1) were placed simultaneously within a large volume ablation cell equipped with a low-volume sampling ring. The laser ablation conditions employed are as follows: energy density of 4–6 J/cm^2, spot sizes were either 25 or 35 μm depending on the size of targeted areas within the zircons, and a repetition rate of 4 Hz. The ablation time was 60 s, and each was preceded and followed by a 45 s background integration interval (within a total washout time of ~120 s). As employed in Chen and Simonetti (2014) and Simonetti and Neal (2010), all of the ablations were conducted using a 1000 mL/min He flow rate. ^{202}Hg, ^{204}(Pb + Hg), ^{206}Pb, ^{207}Pb, and ^{208}Pb ion signals were measured simultaneously on 5 discrete dynode secondary electron multipliers (3 equipped with retardation filters for ^{206}Pb, ^{207}Pb, ^{208}Pb) whereas ^{232}Th, ^{235}U, and ^{238}U ion signals were recorded

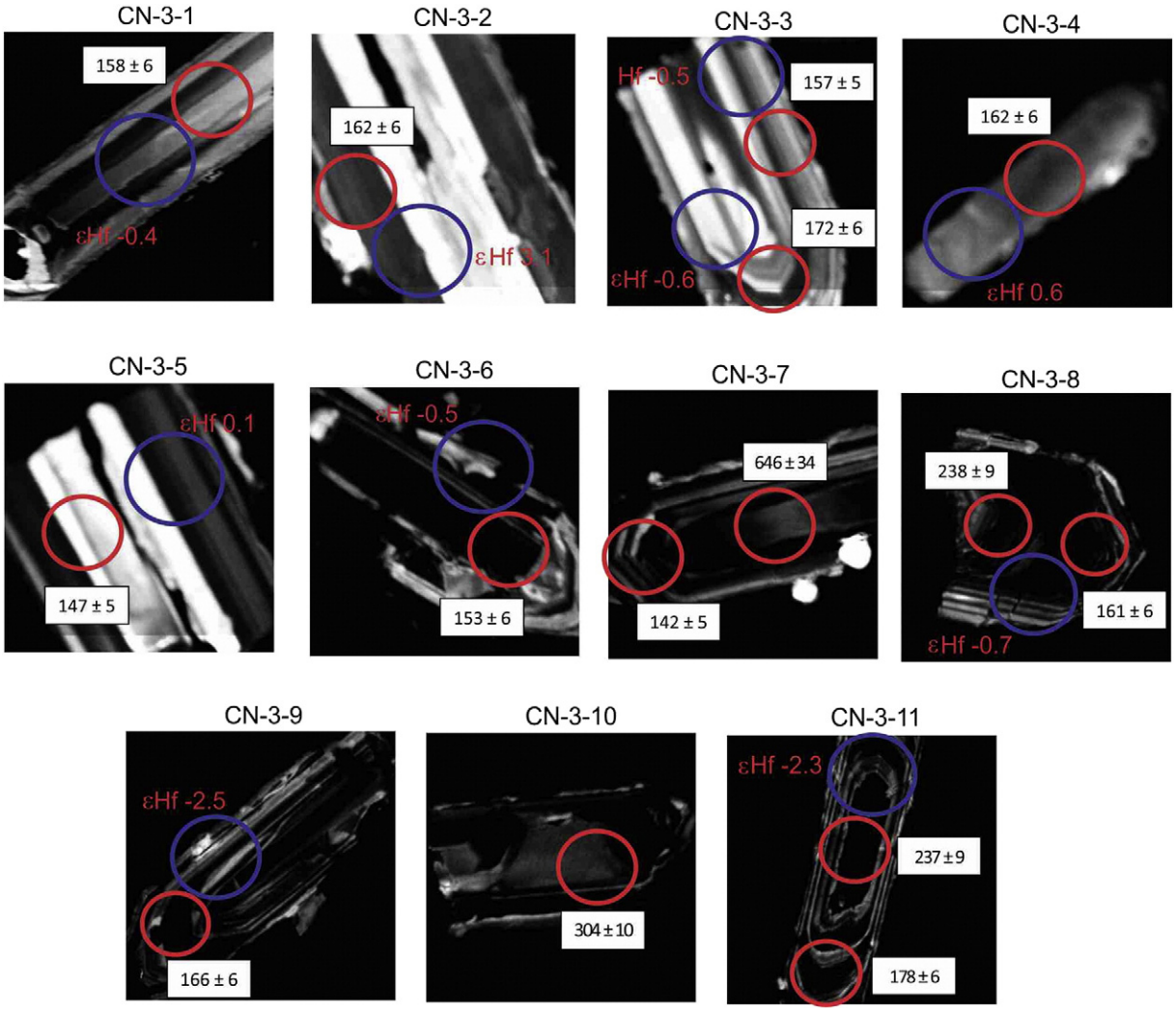

Fig. 6. CL images of zircon grains investigated from sample CN-3 (red circles: U–Pb (^{207}Pb/^{235}U in Ma) spots-25 μm, blue circles: Hf spots-35 μm).

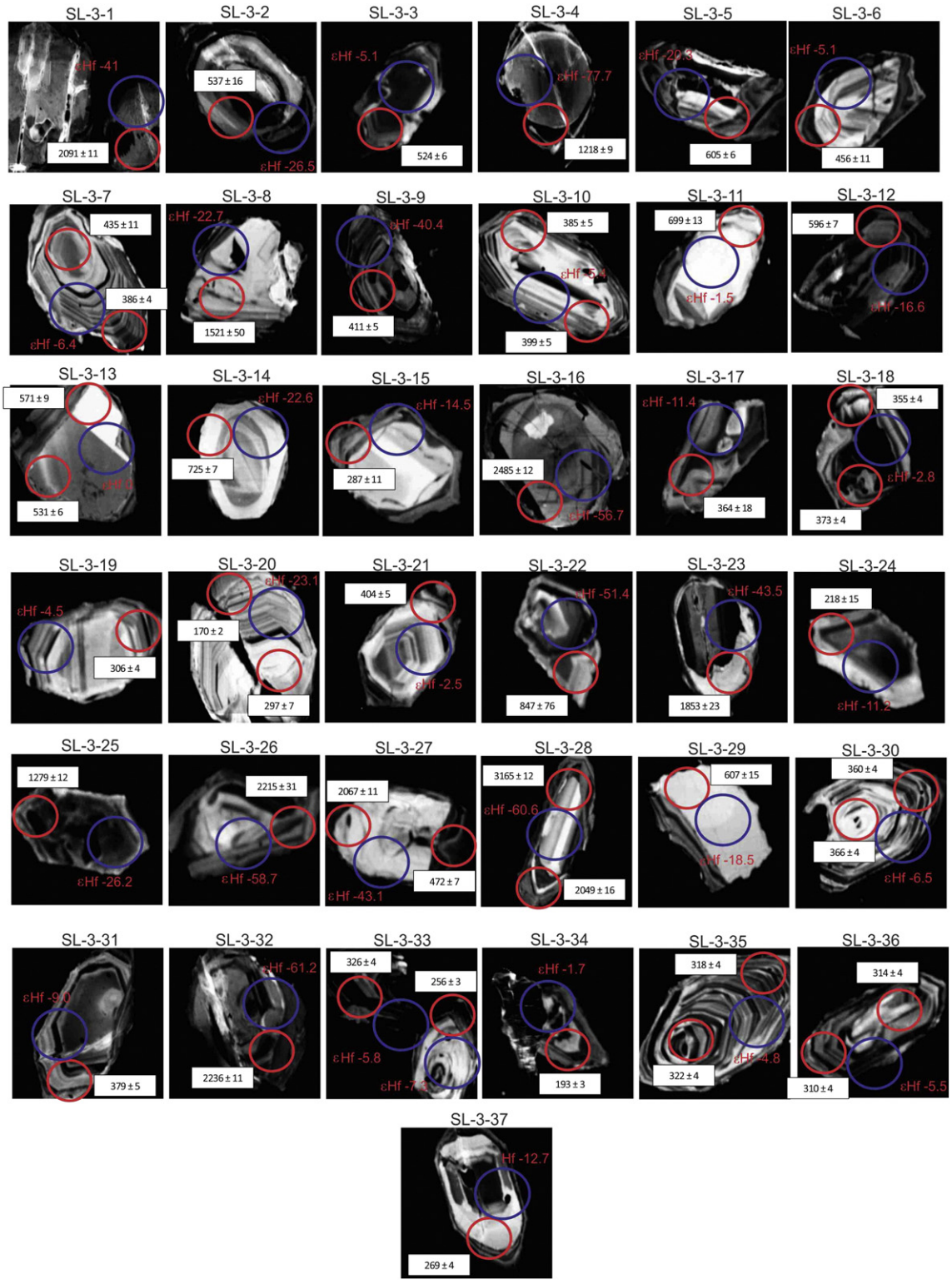

Fig. 7. CL images of zircon grains investigated from sample SL-3 (red circles: U–Pb ($^{207}Pb/^{235}U$ in Ma) spots-25 μm, blue circles: Hf spots-35 μm).

on Faraday cups. Additionally, the ^{202}Hg ion signal was measured in order to correct for the ^{204}Hg interference on ^{204}Pb ($^{204}Hg/^{202}Hg = 0.229883$). Four analyses of the Plešovice (Slama et al., 2008) and 91500 (Wiedenbeck et al., 1995) zircon standards were performed both prior and subsequent each 10 unknown analyses in order to monitor and correct for instrumental drift and laser induced elemental fractionation (LIEF). Hg, Pb, and U ion signals were acquired using the Time-Resolved Analysis (TRA) software (Nu Instruments) and Excel © compatible csv files were imported into the Iolite (v3.1) data reduction software (Paton et al., 2010). The Iolite software corrects for down-hole elemental fractionation (ratios) that can occur with time during laser ablation (Paton et al., 2010). It is well established that several parameters such as laser wavelength, spot size, cell volume, gas flows, and ablation gas can affect the down-hole fractionation (e.g., Horn et al., 2000; Jackson

et al., 2004; Paton et al., 2010). All of the processed data were subsequently imported into the Excel-based macro IsoPlot 4.11 (Ludwig, 2008) for plotting of data on Concordia diagrams (Tera and Wasserburg, 1972), and calculation of either concordant, lower intercept, and/or $^{206}Pb/^{238}U$ weighted mean ages.

4.3. Hf isotopes

The same zircon grains that were investigated for their U–Pb ages were also analyzed for in situ Hf isotope composition. Three well established and recognized zircon standards, Plešovice (Slama et al., 2008), 91500 (Woodhead and Hergt, 2005), and BR266 (Woodhead et al., 2004) were analyzed before the analytical sessions in order to validate and ensure the accuracy of the in-situ Hf results reported here (Tables 4 and 5).

The identical LA-MC-ICP-MS combined instrument configuration was employed for the in-situ Hf analyses as that used for the in-situ U–Pb analyses. The samples and zircon standards (Plešovice, 91500, and BR266) were placed together in a large volume ablation cell equipped with a low-volume sampling ring. The laser ablation conditions employed were as follows: energy density of 4–6 J/cm^2, spot size was 35 μm and a repetition rate of 7 Hz. The ablation time was 60 s, which followed a 30 s background integration interval within a total washout time of ~120 s. All of the ablations were conducted using a 1000 mL/min He flow rate within the ablation cell.

^{183}Ta, ^{181}W, ^{180}Hf, ^{178}Hf, ^{176}Hf, ^{175}Lu, ^{176}Hf, ^{173}Yb, and ^{171}Yb ion signals were measured simultaneously on nine Faraday collectors. The ^{175}Lu ion signal was measured in order to correct for the ^{176}Lu interference on ^{176}Hf ($^{175}Lu/^{176}Lu = 37.61$). Moreover, the ^{176}Yb ion signal interference was determined by assuming the mass bias fractionation factor for Yb (based on measured $^{172}Yb/^{173}Yb$) was equal to that of Hf (e.g., Pearson et al., 2008). Ion signal intensity data were processed using the TRA software (Nu Instruments).

In relation to calculating the age-corrected, initial $^{176}Hf/^{177}Hf$ ratios, the $^{176}Lu/^{176}Hf$ ratios (0.00010–0.00363) are very low for all analyses reported here (Tables 4 and 5). Due to the extremely low $^{176}Lu/^{176}Hf$ ratios in the zircons, present-day, measured $^{176}Hf/^{177}Hf$ ratios are almost identical to their initial values since the magnitude of the correction is within the internal precision (2σ level) for individual analyses (e.g., Schmidberger et al., 2005).

5. Results

5.1. Whole-rock geochemistry

Highly variable LOI (loss on ignition) values were observed in the magmatic rocks (1.6–5.6 wt.%; Table 1), and may be attributed to low-grade alteration as noted in petrographic observations. Therefore, the trace elements (that are considered immobile during low-grade alteration (Ti, Zr, rare earth elements; e.g., Floyd and Winchester, 1978; Pearce and Cann, 1973) were adopted for geochemical evaluation. The collected samples from the CP mostly plot within the gabbroic diorite, granodiorite (extrusive equivalent: dacite porphyry), and granite fields based upon the classification scheme (Winchester and Floyd, 1977; Fig. 8). The Zr/TiO_2 and Nb/Y values for the different rock groups may be subdivided respectively: gabbroic diorites (71.75–176.23) and (0.06–0.25), dacite porphyry (352.27–394.05) and (0.47–0.54), granite (386.66–750.76) and (0.24–0.96). All rock groups are characterized by negative Nb anomalies and depleted in high-field strength elements (HFSE) relative to Th and La in the N-MORB-normalized multi-element plots (Fig. 9A). A negative Ti anomaly is present in most samples. In the chondrite normalized rare earth element (REE) diagrams (Fig. 9B), the samples display enrichments in light REEs (LREEs) over heavy REEs (HREEs) (e.g., $[La/Yb]_N = 1.67–6.21$ for gabbroic diorites, 11.91–12.54 for dacite porphyries, 4.62–20.83 for granites; N: chondrite-normalized).

Dehydration and melting of oceanic crust during subduction can cause element transfer between slab and arc-generated magmas (Gorton and Schandl, 2000). In this context, Th and Nb can provide important insights into the source characteristics (Pearce and Peate, 1995). Enrichment of Th over Nb is one of the typical geochemical characteristics of arc-derived magmas compared to those generated in the other tectonic environments. One possible explanation for the low Nb (and Ta) abundances observed in subduction-derived magmas is the retention of these elements by Ti-rich mineral phases (such as rutile) in the subducted slab (Pearce et al., 2005). The high Th/Nb ratios of the samples may suggest, therefore, generation of CP lithologies in an arc-related setting ($[Th/Nb]_N = 5.88–33.17$ for gabbroic diorites, 28.40–31.96 for dacite porphyries, 18.53–50.56 for granites; N:NMORB-normalized). Furthermore, all of the igneous rocks from CP display similar geochemical patterns compared with volcanic arc granites (Fig. 9A; Pearce et al., 1984). It is well established that volcanic arc granites can form in complexes that range from tholeiitic through calc-alkaline to shoshonitic in composition (Miyashiro, 1974; Pearce et al., 1984). The Ta–Y tectonomagmatic discrimination diagram (Pearce et al., 1984) also supports this notion, in which the magmatic rocks of the CP display low Ta and Y abundances similar to those of volcanic arc granites (Fig. 10A); Ta contents range between 0.1 and 0.7 ppm for gabbroic diorites, 0.6 and 0.7 ppm for dacite porphyries and 0.2–1 ppm for granites (Fig. 10B). In summary, the geochemical characteristics for the igneous rocks from CP investigated here are consistent with arc magmatism. Additionally, the high Th/Nb ratios and enriched LREE signatures relative to HFSEs and HREEs are consistent with subduction-modified mantle source characteristics (Fig. 9A, B; Pearce and Peate, 1995); i.e., there is contribution of a slab-derived component, which is typical of magmas generated in subduction-related settings (Pearce and Peate, 1995).

Th/Hf vs. Ta/Hf discrimination diagram is used to delineate the type of arc magmatism (Schandl and Gorton, 2002; Fig. 10C, D). The solubility of Th is very low in subduction zones and higher Th/Ta ratios (3.33–23) may be attributed to a greater contribution from a sedimentary component within arc magmas (Gorton and Schandl, 2000). The higher Th/Hf (0.34 to 3.78) and lower Ta/Hf (0.03 to 0.31) ratios reported for the CP rocks investigated here (Fig. 10C, D) suggest magma generation within a continental arc setting. Additionally, this interpretation is consistent with the compositional fields denoted within Nb/Y (0.05–0.96) vs. Zr/Y (1.65–12.43) and Th/Yb (0.35–16.58) vs. Nb/Yb (0.61–10.96) discrimination diagrams (Fig. 11; Condie and Kroner, 2013).

5.2. U–Pb geochronology

U–Pb geochronometers have been successfully applied to date magmatic rocks, which formed from a few million years to more than billions of years ago (e.g., Schmidberger et al., 2005; Simonetti and Neal, 2010). Recently, in-situ U–Pb dating of accessory minerals by LA-MC-ICP-MS has become a more widely practiced technique since spatial resolution allows for accurate dating of core vs. rim regions of single mineral grains by using small laser spot sizes (e.g., ≤40 μm; Simonetti et al., 2005). Moreover, it is cheaper and is characterized by a rapid analysis time with a simple sample preparation process compared with Isotope Dilution Thermal Ionization Mass Spectrometry (ID-TIMS) and Secondary Ion Mass Spectrometry (SIMS) techniques. In contrast, bulk zircon analysis will result in the masking of distinct magmatic events and possibly metamorphic overgrowths present at the micron-scale.

There is a lack of published radiometric age data for any of the units belonging to the CP. In this study, zircons obtained from dacite porphyry (CN-3) and granite (SL-3) samples yield Middle Jurassic ages of 161 ± 6 Ma for CN-3 (concordant age), 168 ± 2 Ma (lower intercept age), and 170 ± 2 Ma (concordant age) for SL-3 (Fig. 12; Tables 2, 3). Figs. 7 and 12c clearly show that many zircons from granite sample SL-3 (#37) contain inherited components yielding much older ages (>170 Ma) and are clearly detrital in origin; these have also experienced recent Pb loss as they plot as discordant data. Zircons of detrital origin

Table 1
Major and trace element compositions of the whole rock samples from the Çangaldağ Pluton.

Sample	SL-1	SL-2	CN-1	CN-9	CN-11	SL-4	SL-5	SL-6	SL-7	SL-8	CN-8	CN-3	SL-3	SL-9	SL-10	SL-11
	Gabbroic diorite										*Dacite porphyry*		*Granite*			
Coordinates	414320N 341954E	414320N 341955E	414225N 345510E	414215N 343524E	414203N 343542E	414314N 341533E	414315N 341537E	414317N 341547E	414323N 341417E	414326N 341419E	414232N 343513E	414224N 343521E	414317N 341956E	414325N 341418E	414325N 341419E	414327N 311419E
SiO_2 (wt.%)	54.30	54.07	51.94	52.24	54.86	53.39	53.59	53.22	52.36	49.44	67.78	66.13	73.54	68.88	72.78	69.96
Al_2O_3	16.43	17.43	14.97	15.33	15.41	17.36	17.32	17.65	15.76	16.39	15.62	15.11	11.76	15.32	14.16	14.62
$Fe_2O_3^t$	7.25	6.82	7.17	6.83	6.73	6.33	6.29	7.79	4.94	9.20	3.28	3.22	1.55	1.27	1.77	2.73
MgO	5.30	4.35	8.13	8.22	6.62	5.85	6.71	4.68	5.47	7.57	1.29	1.11	0.50	0.91	0.60	1.05
CaO	6.87	6.32	6.99	6.82	5.36	7.19	7.25	7.99	14.31	8.86	1.29	2.95	3.03	3.81	1.80	1.69
Na_2O	4.50	3.60	3.44	2.97	3.61	5.00	3.46	3.69	3.07	3.67	3.88	3.38	2.67	6.41	4.50	4.25
K_2O	0.81	1.40	0.54	1.38	1.59	0.89	1.60	0.68	0.35	0.83	2.41	2.56	1.92	0.59	1.68	3.16
TiO_2	0.85	1.05	0.69	0.63	0.84	0.84	0.77	2.00	0.91	1.42	0.44	0.37	0.15	0.49	0.13	0.40
P_2O_5	0.11	0.18	0.11	0.08	0.12	0.10	0.09	0.29	0.05	0.15	0.15	0.12	0.15	0.10	0.07	0.07
MnO	0.13	0.14	0.12	0.12	0.13	0.09	0.09	0.14	0.11	0.16	0.06	0.08	0.04	0.03	0.04	0.02
Cr_2O_3	0.03	0.02	0.06	0.07	0.05	0.02	0.04	0.00	0.02	0.03	0.01	0.00	0.01	0.01	0.01	0.01
LOI	3.20	4.40	5.60	5.10	4.50	2.80	2.60	1.60	2.50	2.00	3.70	4.90	4.60	2.10	2.40	2.00
Sum	99.80	99.79	99.80	99.77	99.82	99.84	99.82	99.80	99.83	99.76	99.92	99.91	99.95	99.93	99.95	99.94
Ba (ppm)	174.00	330.00	87.00	258.00	177.00	86.00	180.00	100.00	38.00	227.00	138.00	249.00	295.00	64.00	133.00	276.00
Ni	22.00	23.00	150.00	139.00	94.00	52.00	77.00	<20	36.00	60.00	<20	<20	<20	<20	<20	<20
Sc	25.00	19.00	22.00	21.00	22.00	23.00	19.00	26.00	33.00	31.00	7.00	6.00	4.00	4.00	2.00	5.00
Co	26.20	23.30	31.70	31.10	25.80	20.70	24.60	22.60	19.60	33.00	7.00	5.00	2.00	2.30	1.60	5.80
Cs	0.40	2.00	0.20	0.70	0.20	0.80	1.60	1.70	0.30	0.80	4.50	3.20	1.80	0.60	2.10	1.20
Ga	15.00	17.20	14.60	14.20	14.50	14.90	15.70	18.20	17.90	15.90	16.90	17.00	8.60	15.00	16.20	15.40
Hf	3.90	4.40	2.30	2.20	3.10	2.50	2.50	3.20	1.70	2.90	4.20	3.90	1.60	5.90	3.20	4.70
Nb	3.40	6.00	3.30	3.70	4.40	2.70	2.40	6.30	3.30	1.50	6.70	6.50	2.20	5.30	8.00	4.70
Rb	24.00	57.10	14.60	51.50	53.50	43.90	73.90	17.90	8.60	22.00	151.10	109.20	61.40	19.70	62.30	91.00
Sr	282.40	362.00	87.90	264.50	64.80	128.00	215.60	343.30	152.80	324.20	55.70	119.80	101.10	118.70	112.60	106.50
Ta	0.20	0.40	0.40	0.40	0.40	0.30	0.30	0.70	0.30	0.10	0.60	0.70	0.20	0.60	1.00	0.50
Th	3.30	6.20	3.90	4.20	5.10	4.40	4.10	3.50	1.00	1.00	9.80	10.70	2.10	13.80	12.10	11.40
U	1.10	2.40	1.40	1.70	2.10	1.70	1.00	1.70	0.60	0.30	3.00	3.80	0.80	5.00	4.10	3.70
V	166.00	152.00	142.00	136.00	148.00	147.00	121.00	251.00	179.00	202.00	45.00	38.00	21.00	52.00	11.00	33.00
W	0.80	0.60	<0.5	1.20	1.30	1.60	1.20	1.00	1.10	<0.5	1.50	3.10	1.80	1.10	0.70	0.60
Zr	149.80	170.90	89.30	85.60	109.00	91.00	94.80	143.50	52.70	119.20	155.00	145.80	58.00	223.70	97.60	180.30
Y	25.80	23.60	17.70	15.50	18.60	16.80	16.90	25.40	32.00	25.80	12.40	13.70	6.80	18.00	8.30	19.50
La	13.90	20.10	10.80	11.60	15.20	8.00	8.80	12.30	7.30	5.70	23.60	24.40	9.90	13.00	21.20	18.00
Ce	32.00	39.60	23.30	22.60	28.80	19.00	18.30	29.50	24.00	16.30	47.40	46.40	18.10	28.40	45.10	38.10
Pr	4.33	4.95	2.83	2.69	3.57	2.44	2.49	3.95	3.39	2.72	5.15	5.23	1.89	3.24	5.05	4.22
Nd	18.40	21.10	11.70	11.10	15.20	10.40	11.10	18.30	16.80	13.70	19.20	18.80	7.20	13.30	18.70	16.40
Sm	4.46	4.23	2.89	2.57	3.31	2.62	2.73	4.79	4.76	3.64	3.59	3.66	1.40	2.97	3.57	3.33
Eu	1.25	1.31	0.86	0.80	0.84	0.94	0.91	1.43	1.04	1.30	0.81	0.76	0.91	1.00	0.59	0.74
Gd	4.78	4.52	3.12	2.79	3.55	3.20	3.01	5.11	5.92	4.68	2.93	3.13	1.38	3.01	2.50	3.41
Tb	0.83	0.73	0.52	0.48	0.58	0.50	0.49	0.78	0.95	0.73	0.44	0.48	0.22	0.48	0.31	0.54
Dy	4.74	4.17	3.19	2.70	3.58	2.97	2.87	4.69	5.83	4.60	2.39	2.51	1.25	3.17	1.56	3.35
Ho	0.98	0.96	0.68	0.60	0.76	0.60	0.60	0.90	1.09	0.94	0.49	0.51	0.29	0.63	0.25	0.63
Er	2.82	2.47	2.05	1.78	2.16	1.67	1.81	2.51	3.15	2.83	1.32	1.51	0.76	1.94	0.76	2.09
Tm	0.43	0.38	0.29	0.24	0.32	0.26	0.25	0.37	0.47	0.41	0.19	0.22	0.12	0.31	0.11	0.29
Yb	2.60	2.32	1.92	1.62	2.12	1.65	1.60	2.36	2.82	2.45	1.35	1.47	0.79	2.02	0.73	1.91
Lu	0.38	0.35	0.29	0.26	0.33	0.27	0.24	0.35	0.41	0.39	0.21	0.23	0.11	0.32	0.12	0.30
$(Th/Nb)_N$	18.85	20.06	22.95	22.04	22.51	31.64	33.17	10.79	5.88	12.94	28.40	31.96	18.53	29.37	47.10	50.56
$(La/Yb)_N$	3.83	6.21	4.03	5.14	5.14	3.48	3.95	3.74	1.86	1.67	11.91	12.54	8.99	4.62	20.83	6.76

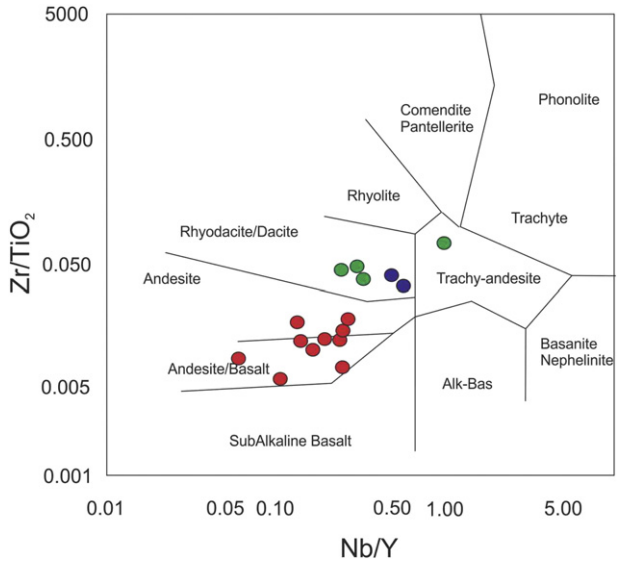

Fig. 8. Geochemical classification of the Çangaldağ Pluton after Winchester and Floyd (1977). Red circles: gabbroic diorites; blue circles: dacite porphyries; green circles: granites.

have variable ages ranging from Archean to Jurassic and their relative distribution is shown in Fig. 13, which involve a variety of different-aged sedimentary sources. Moreover, the in-situ U–Pb age results reported here indicate multiple periods of zircon growth during significant geological/tectonic events known to have occurred within the study area. For example, the possible source of this magmatism can be the Devrekani Metamorphics (a member of the Variscan basement; Figs. 1, 2, 3), which contain mostly paragneisses (including zircon minerals from 293 to 668 Ma), amphibolite and orthogneisses (age is between 316 and 252 Ma; Gücer et al., 2016). In contrast, the zircons from dacite porphyry sample (#11) exhibit a more consistent age data distribution (between 142 and 304 Ma) compared to the granite sample, which may be attributed to the derivation from an igneous source rather than a sedimentary origin (Fig. 6, Table 3).

5.3. Hf isotope systematics

The Lu–Hf geochronometer is an effective tool used to evaluate mantle source(s) and determine radiometric ages and depleted mantle model age(s) (T_{DM}) of igneous rocks (e.g., Schmidberger et al., 2005). Additionally, combining in-situ U–Pb age determinations with corresponding Hf isotope compositions within the same zircons provides significant information in relation to the source(s) of magma. Given that zircon is a refractory mineral and a major reservoir of Hf in most crustal rocks, then Hf isotope ratios can be used to understand the evolution of the crust (e.g., Batumike et al., 2007).

In this study, the same zircon grains obtained from dacite porphyry (CN-3) and granite (SL-3) samples within the CP were analyzed for their Hf isotope compositions. The in-situ, initial $^{176}Hf/^{177}Hf$ ratios of two concordant mid-Jurassic zircon grains are 0.28276 ± 0.00003 and 0.28213 ± 0.00002 for the dacite porphyry (161 ± 6 Ma; concordant age) and granite (170 ± 2 Ma; concordant age) samples, respectively. In Fig. 14, which displays age vs. their corresponding initial $^{176}Hf/^{177}Hf$ ratios, the zircons investigated here plot predominantly between Depleted Mantle (DM) and Chondritic Uniform Reservoir (CHUR) development lines. These results are consistent with zircon formation from relatively juvenile magmas, whereas εHf compositions that plot below CHUR suggest recycling of pre-existing crustal material (Batumike et al., 2007). The zircon (CN-3-8; Table 4) from the dacite porphyry sample (CN-3) that yields a concordant, Middle Jurassic age of 161 ± 6 Ma contains a relatively homogenous initial $^{176}Hf/^{177}Hf$ ratio close to $CHUR_{(161\ Ma)}$ (0.28279; Fig. 14A; Bouvier et al., 2008). The other concordant zircon grain SL-3-20, which yields an age of 170 ± 2 Ma (Fig. 14C), is characterized by an initial Hf isotope composition that is lower than the value for $CHUR_{(170\ Ma)}$; this may be attributed to crustal input during magma genesis. The Hf isotope compositions for the concordant zircons from the dacite porphyry and granite samples correspond to T_{DM} model ages of 674 and 1512 Ma ages (for Middle Jurassic magmatism; Fig. 14A, C), respectively. These model ages suggest that magmatism associated with the CP may have involved partial melting of Neoproterozoic/Mesoproterozoic crustal rocks, such as Devrekani Metamorphics in the study area, which are common in Gondwana-derived terranes (Göncüoğlu, 2010; Rapela et al., 2016). The εHf values (Fig. 14B, D; Tables 4, 5) of these concordant zircon grains are −0.7 and −23.1 for the dacite porphyry and granite samples, respectively, which may be explained by mixing of depleted mantle and crustal sources (e.g., Kröner et al., 2014). Also, the wide range of εHf values (0 to −77.7) recorded for individual zircon grains from granite sample SL-3 confirm their predominant sedimentary sources (Fig. 14D), whereas the narrower range of εHf data (3.1 to −2.5) for the dacite porphyry sample is consistent with their derivation from a higher amount of juvenile material (Fig. 14B). Zircons from granite sample SL-3 are characterized mainly by negative εHf values and plot below the CHUR

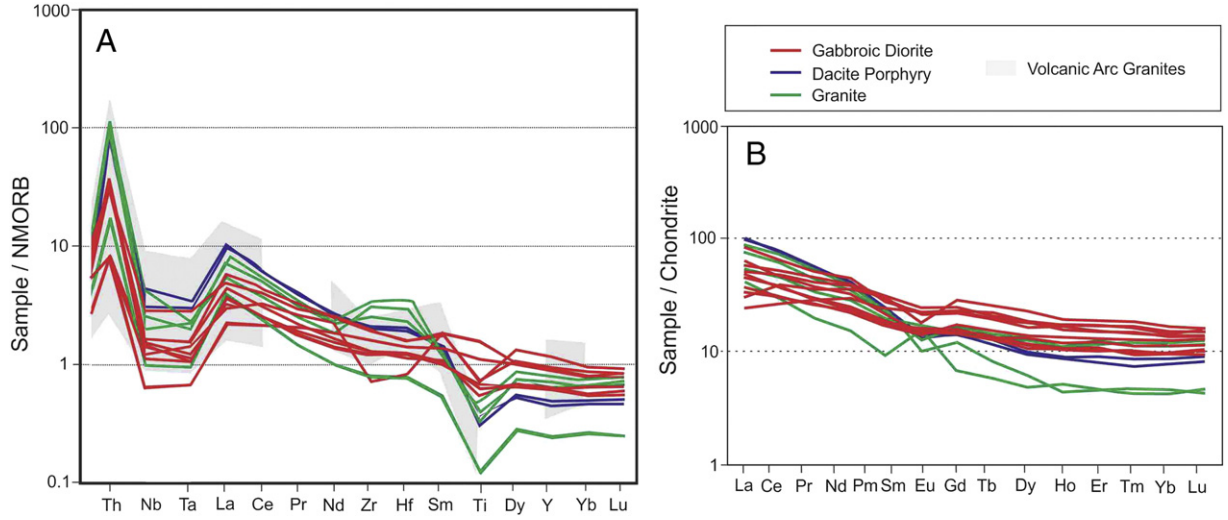

Fig. 9. (A) N-MORB normalized multi-element spider diagram. (B) Chondrite normalized rare earth element spider diagram. N-MORB and chondrite normalization values are from Sun and McDonough (1989). Volcanic Arc Granites data from Pearce et al. (1984).

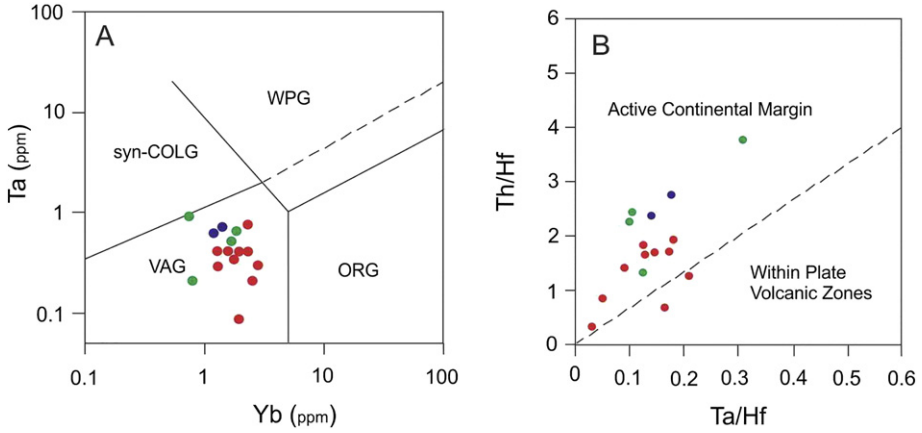

Fig. 10. (A) Geotectonic discrimination diagrams for the Çangaldağ Pluton. (B) Pearce et al. (1984). (C) Schandl and Gorton (2002). Symbols same as in Fig. 9.

development line, which is consistent with the involvement of crustal rocks in their generation; some of the older zircons plot on or proximal to the CHUR development line, which may indicate the participation of a juvenile magma component (e.g., Batumike et al., 2007).

6. Discussion of geodynamic implications

The new whole rock geochemical results, zircon U–Pb ages, and Hf isotope data reported here for the CP plutonic rocks allow for a reassessment of the geodynamic evolution of the CPSC. The Central Pontides include several pre-Late Jurassic intrusions including the Sivrikaya, Deliktaş Devrekani, and Karaman plutons as well as the Ağlı and Sallamadağ porphyric stocks. U–Pb dating of zircons from Sivrikaya and Deliktaş plutons has yielded Carboniferous and Permian ages (303–275 Ma; Nzegge, 2008), respectively. These data clearly indicate that a group of intrusions within the CP is related to a Variscan magmatic event. Nzegge (2008) also suggested that the Sivrikaya Granitoid formed as a result of lithospheric slab break-off and/or lithospheric delamination/collapse processes. Subsequently, uprising of hot asthenosphere caused the emplacement of purely crustal-derived peraluminous, S-type Deliktaş Granitoid until the Early Permian.

The first Middle Jurassic radiometric age data (176 ± 7 Ma and 162 ± 5 Ma) was obtained by K–Ar dating of the Asarcık Diorite (Yılmaz and Bonhomme, 1991). These results corroborate field evidences since both intrude the Triassic Küre Complex, and are unconformably overlain by the Upper Jurassic Limestones (Boztuğ and Yılmaz, 1995). The magmatism was interpreted as the product of northward subduction of the Paleotethyan oceanic crust beneath the Eurasian Plate (Boztuğ and Yılmaz, 1995). Conversely, Jurassic-aged magmatism (e.g. Devrekani and Asarcık Granitoids) was interpreted as a product of the southward subduction of the Küre Basin (Nzegge, 2008; Ustaömer and Robertson, 1999), which was still open during the Carnian–Norian (Kozur et al., 2000). Recently, Okay et al. (2014) suggested an extensional magmatic arc tectonic setting for the Middle Jurassic metamorphism and magmatism in the Central Pontides, which is responsible for the generation of the Karaman pluton and Ağlı and Sallamadağ porphyries.

The presence of Jurassic magmatic rocks is also known in the western part of SCT, Eastern Pontides, Crimea (Ukraine), Caucasus, and Iran. For example, in the western SCT, the Lower to Middle Jurassic Mudurnu volcanics are composed of mafic and felsic volcanic rocks interbedded with volcaniclastics, mudstone, and limestone. They are overlain by the Late Jurassic–Early Cretaceous Soğukçam Limestone (Genc and Tüysüz, 2010). Geochemically, the Mudurnu volcanics exhibit subalkaline and calc-alkaline affinity and are interpreted as the result of rift-related magmatism (Genc and Tüysüz, 2010). Further to the east, in the Eastern Pontides (e.g. Artvin-Yusufeli area), the Early Jurassic Demirkent Complex intrudes the Carboniferous metamorphic basement rocks of the SCT (e.g. Dokuz et al., 2010). These magmatic rocks display calc-alkaline and tholeiitic affinity and are interpreted as products of a continental rift environment (Dokuz et al., 2010). Recently, Late Jurassic magmatism has been reported in the Eastern Sakarya Zone and interpreted as evidence for the slab breakoff of Paleotethyan oceanic lithosphere (Dokuz et al., 2017). Şen (2007) proposed that the

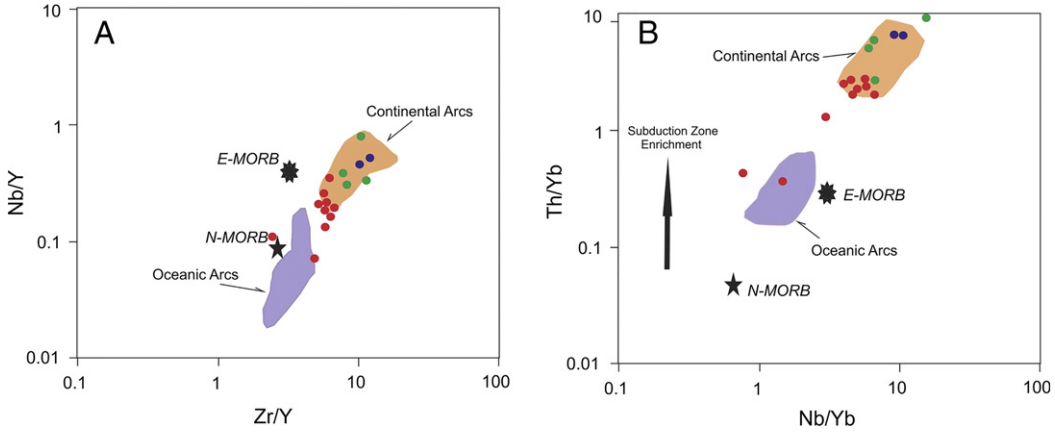

Fig. 11. (A) Nb/Y vs Zr/Y and (B) Th/Yb vs Nb/Yb diagrams. Oceanic Arc and Continental Arcs values are from Condie and Kroner (2013). Average N-MORB and E-MORB values are from Sun and McDonough (1989). Symbols same as in Fig. 9.

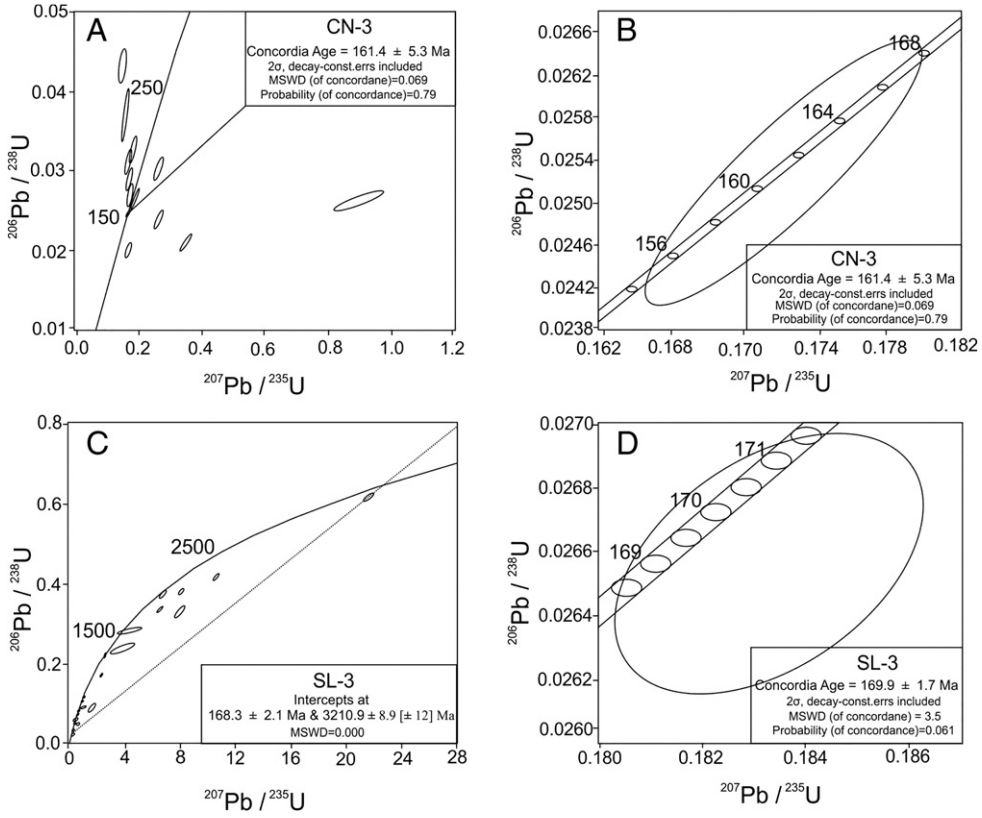

Fig. 12. $^{206}Pb/^{238}U$ vs $^{207}Pb/^{235}U$ diagrams for CN-3 and SL-3 samples. (a) Concordia age for CN-3. (b) Concordia spot (analysis # 15) for CN-3. (c) Lower intercept age for SL-3. (d) Concordia age for SL-3 (analysis # 48).

Jurassic volcanics from the Eastern Pontides to the south of Trabzon region have been formed in an intra-arc rift. Jurassic arc-type volcanic rocks including tholeiitic basalts and evolved andesitic-rhyolites were also reported from Crimea (Meijers et al., 2010). These were generated in a subduction-related setting within the overriding plate, indicating a period of northward subduction beneath the Eurasian margin (Meijers et al., 2010). Moreover, subduction-related Jurassic volcanic rocks (basalts, andesites and rhyolites) were identified in the Greater Caucasus (McCann et al., 2010). All of these occurrences from the western part of SCT through to the Central-Eastern Pontides, and Crimea to Caucaus are related to Jurassic continental arc magmatism, and suggest that subduction occurred beneath the Cimmerian Terrane during the Jurassic.

In the Central Pontides, the CP occurs between the Alpine SCT and the CPSC. It was commonly accepted that the CPSC consists mainly of the oceanic remnants of Paleotethys (e.g. Elmas and Yiğitbaş, 2001; Robertson and Ustaömer, 2004; Şengör and Yılmaz, 1981; Tüysüz, 1999). Recent radiometric age data, however, indicate that the formation and metamorphic ages of the CPSC-units are Middle Jurassic and Early Cretaceous, respectively (e.g. Çimen, 2016; Göncüoğlu et al., 2008, 2012, 2014; Marroni et al., 2014; Okay et al., 2006, 2013, 2014). Sayit et al. (2016) have recently shown that the CPSC-units (e.g. Arkot Dağ, Domuz Dağ, Aylı Dağ) are mainly supra-subduction-type and were formed by northward subduction of the Intra-Pontide oceanic crust. The radiolarian data from basalt–chert associations prove that this ocean was open from the Mid-Late Triassic (Arkot Dağ Melange; Tekin et al., 2012) until the early Late Cretaceous (Göncüoğlu et al., 2014). The most recent U–Pb radiometric age data from the CMC, which is the northernmost unit of the CPSC and in tectonic contact

Table 2
U–Pb isotopic data for zircons in the dacite porphyry sample.

Grain #	^{238}U (V)	^{206}Pb (cps)	$^{206}Pb/^{204}Pb$	$^{206}Pb/^{238}U$	2σ	$^{207}Pb/^{235}U$	2σ	$^{207}Pb/^{206}Pb$	2σ	$^{206}Pb/^{238}U$ age (Ma)	$^{207}Pb/^{235}U$ age (Ma)	$^{207}Pb/^{206}Pb$ age (Ma)
CN-3-1	0.0810	98,563	1000	0.0200	0.0190	0.1684	0.0062	0.0384	0.0094	127 ± 120	158 ± 6	343 ± 420
CN-3-2	0.1194	153,063	3,000,000	0.0271	0.0250	0.1731	0.0063	0.0322	0.0088	172 ± 160	162 ± 6	621 ± 390
CN-3-3-1	0.1140	153,938	1,000,000	0.0325	0.0300	0.1845	0.0066	0.0294	0.0081	206 ± 190	172 ± 6	743 ± 360
CN-3-3-2	0.0682	90,125	1,000,000	0.0309	0.0290	0.1679	0.0062	0.0255	0.0068	196 ± 180	157 ± 5	919 ± 300
CN-3-4	0.1296	162,500	230,000	0.0290	0.0270	0.1734	0.0067	0.0240	0.0062	184 ± 170	162 ± 6	986 ± 280
CN-3-5	0.1185	145,625	200,000	0.0355	0.0330	0.1559	0.0057	0.0210	0.0052	224 ± 210	147 ± 5	1121 ± 230
CN-3-6	0.1304	153,875	340,000	0.0385	0.0360	0.1630	0.0061	0.0209	0.0051	244 ± 230	153 ± 6	1126 ± 230
CN-3-7-1	0.0899	109,750	700,000	0.0430	0.0410	0.1503	0.0055	0.0178	0.0043	270 ± 250	142 ± 5	1266 ± 190
CN-3-7-2	0.2164	263,625	6640	0.0261	0.0240	0.8970	0.0630	0.2610	0.0660	166 ± 150	646 ± 34	3174 ± 390
CN-3-8-1	0.1759	208,000	25,000	0.0253	0.0230	0.1722	0.0062	0.0513	0.0130	160 ± 150	161 ± 6	252 ± 580
CN-3-8-2	0.1711	202,500	35,000	0.0238	0.0220	0.2651	0.0100	0.0790	0.0200	151 ± 140	238 ± 9	1168 ± 510
CN-3-9	0.0869	110,500	31,000	0.0258	0.0240	0.1786	0.0065	0.0503	0.0130	164 ± 150	166 ± 6	208 ± 580
CN-3-10	0.2347	217,688	8020	0.0208	0.0190	0.3504	0.0130	0.1311	0.0330	132 ± 120	304 ± 10	2102 ± 450
CN-3-11-1	0.1430	190,313	28,000	0.0265	0.0240	0.1918	0.0070	0.0514	0.0130	168 ± 150	178 ± 6	255 ± 570
CN-3-11-2	0.2355	353,750	67,000	0.0302	0.0280	0.2643	0.0110	0.0616	0.0150	191 ± 170	237 ± 9	650 ± 520

Table 3
U–Pb isotopic data for zircons in the granite sample.

Grain #	^{238}U (V)	^{206}Pb (cps)	$^{206}Pb/^{204}Pb$	$^{206}Pb/^{238}U$	2σ	$^{207}Pb/^{235}U$	2σ	$^{207}Pb/^{206}Pb$	2σ	$^{206}Pb/^{238}U$ age (Ma)	$^{207}Pb/^{235}U$ age (Ma)	$^{207}Pb/^{206}Pb$ age (Ma)
SL-3-1	0.0080	241,688	17,000	0.3756	0.0046	6.8410	0.0860	0.1320	0.0004	2056 ± 22	2091 ± 11	2123 ± 6
SL-3-2	0.0127	62,125	8700	0.0811	0.0034	0.7040	0.0250	0.0613	0.0005	501 ± 20	537 ± 16	641 ± 17
SL-3-3	0.0398	170,375	16,000	0.0824	0.0012	0.6760	0.0098	0.0600	0.0003	510 ± 7	524 ± 6	600 ± 11
SL-3-4	0.0823	689,375	134,000	0.1718	0.0023	2.3210	0.0320	0.0979	0.0003	1021 ± 12	1218 ± 9	1582 ± 5
SL-3-5	0.0247	135,688	20,000	0.0963	0.0012	0.8145	0.0110	0.0615	0.0003	592 ± 7	605 ± 6	655 ± 9
SL-3-6	0.0510	185,313	40,000	0.0714	0.0019	0.5700	0.0170	0.0580	0.0003	444 ± 12	456 ± 11	527 ± 10
SL-3-7-1	0.1082	315,625	102,000	0.0612	0.0008	0.4627	0.0057	0.0548	0.0002	383 ± 5	386 ± 4	403 ± 8
SL-3-7-2	0.0679	189,813	32,000	0.0610	0.0013	0.4500	0.1100	0.0577	0.0007	381 ± 8	435 ± 24	510 ± 27
SL-3-8	0.0254	321,250	81,000	0.2389	0.0098	3.8300	0.7500	0.1066	0.0016	1378 ± 51	1521 ± 50	1731 ± 27
SL-3-9	0.0246	84,625	16,700	0.0600	0.0008	0.5003	0.0075	0.0598	0.0004	375 ± 5	411 ± 5	593 ± 13
SL-3-10-1	0.0392	128,813	Infinite	0.0630	0.0009	0.4822	0.0072	0.0552	0.0003	394 ± 5	399 ± 5	418 ± 12
SL-3-10-2	0.0128	52,250	Infinite	0.0603	0.0008	0.4620	0.0069	0.0554	0.0004	377 ± 5	385 ± 5	424 ± 15
SL-3-11	0.0005	33,063	Infinite	0.1063	0.0014	0.9960	0.0260	0.0671	0.0011	651 ± 8	699 ± 13	830 ± 32
SL-3-12	0.0175	103,188	Infinite	0.0962	0.0014	0.7998	0.0120	0.0600	0.0003	591 ± 8	596 ± 7	601 ± 12
SL-3-13-1	0.0013	30,588	Infinite	0.0882	0.0011	0.7690	0.0210	0.0614	0.0007	544 ± 7	571 ± 9	639 ± 23
SL-3-13-2	0.0074	53,375	Infinite	0.0844	0.0013	0.6874	0.0100	0.0590	0.0004	522 ± 8	531 ± 6	563 ± 13
SL-3-14	0.0013	40,500	Infinite	0.1161	0.0015	1.0520	0.0180	0.0649	0.0005	707 ± 9	725 ± 7	767 ± 15
SL-3-15	0.0328	61,313	Infinite	0.0336	0.0005	0.3290	0.0150	0.0718	0.0031	212 ± 3	287 ± 11	918 ± 83
SL-3-16	0.0316	721,875	300,000	0.4165	0.0052	10.5670	0.1300	0.1837	0.0005	2245 ± 24	2485 ± 12	2685 ± 4
SL-3-17	0.0260	69,938	Infinite	0.0531	0.0025	0.4400	0.0250	0.0592	0.0007	333 ± 16	364 ± 18	571 ± 24
SL-3-18-1	0.1373	386,875	22,000	0.0593	0.0007	0.4449	0.0055	0.0546	0.0002	371 ± 4	373 ± 4	395 ± 7
SL-3-18-2	0.1379	366,875	34,000	0.0560	0.0007	0.4190	0.0058	0.0545	0.0002	350 ± 5	355 ± 4	388 ± 9
SL-3-19	0.0461	114,313	7400	0.0484	0.0006	0.3524	0.0048	0.0529	0.0002	304 ± 4	306 ± 4	324 ± 11
SL-3-20-1	0.0676	89,313	11,000	0.0265	0.0003	0.1834	0.0024	0.0500	0.0003	168 ± 2	170 ± 2	197 ± 13
SL-3-20-2	0.0335	76,375	11,500	0.0441	0.0011	0.3420	0.0097	0.0562	0.0004	278 ± 7	297 ± 7	457 ± 14
SL-3-21	0.0237	87,375	80,000	0.0635	0.0009	0.4888	0.0071	0.0562	0.0003	396 ± 5	404 ± 5	460 ± 12
SL-3-22	0.0902	373,750	80,000	0.0896	0.0076	1.6300	0.1700	0.1076	0.0059	545 ± 45	847 ± 76	1520 ± 130
SL-3-23	0.0199	299,375	66,000	0.2828	0.0072	4.3800	0.7400	0.1271	0.0007	1602 ± 36	1853 ± 23	2056 ± 10
SL-3-24	0.0861	110,500	80,000	0.0280	0.0004	0.2620	0.0710	0.0541	0.0010	178 ± 3	218 ± 15	359 ± 36
SL-3-25	0.0049	100,500	21,000	0.2198	0.0049	2.5500	0.0680	0.0834	0.0007	1279 ± 27	1279 ± 22	1276 ± 17
SL-3-26	0.0453	752,500	640,000	0.3290	0.0110	7.9700	0.2700	0.1758	0.0006	1827 ± 52	2215 ± 31	2612 ± 5
SL-3-27-1	0.0056	203,000	Infinite	0.3714	0.0046	6.6590	0.0830	0.1296	0.0004	2035 ± 22	2067 ± 11	2092 ± 5
SL-3-27-2	0.0463	118,125	160,000	0.0488	0.0007	0.5930	0.0110	0.0878	0.0006	307 ± 4	472 ± 7	1379 ± 14
SL-3-28-1	0.0586	980,000	7,000,000	0.3350	0.0045	6.5420	0.1200	0.1413	0.0013	1862 ± 21	2049 ± 16	2240 ± 15
SL-3-28-2	0.0083	413,125	Infinite	0.6174	0.0076	21.6020	0.2700	0.2521	0.0006	3099 ± 30	3165 ± 12	3197 ± 4
SL-3-29	0.0037	40,875	Infinite	0.0913	0.0012	1.0200	0.1600	0.0621	0.0008	563 ± 7	607 ± 15	658 ± 21
SL-3-30-1	0.0789	217,813	Infinite	0.0562	0.0007	0.4254	0.0055	0.0546	0.0002	352 ± 5	360 ± 4	396 ± 9
SL-3-30-2	0.0496	145,375	200,000	0.0573	0.0007	0.4341	0.0057	0.0548	0.0002	359.3 ± 4	366 ± 4	400 ± 9
SL-3-31	0.0560	167,250	Infinite	0.0599	0.0008	0.4535	0.0064	0.0545	0.0002	374 ± 5	379 ± 5	390 ± 9
SL-3-32	0.0293	616,250	Infinite	0.3800	0.0047	8.0470	0.1000	0.1535	0.0004	2076 ± 22	2236 ± 11	2384 ± 5
SL-3-33-1	0.0911	222,875	13,000	0.0505	0.0007	0.3799	0.0051	0.0545	0.0002	317 ± 4	326 ± 4	389 ± 8
SL-3-33-2	0.0545	105,688	13,100	0.0383	0.0005	0.2862	0.0041	0.0546	0.0003	242 ± 3	256 ± 3	394 ± 12
SL-3-34	0.0878	122,563	20,000	0.0288	0.0004	0.2095	0.0028	0.0527	0.0003	183 ± 3	193 ± 3	314 ± 13
SL-3-35-1	0.0987	239,188	Infinite	0.0499	0.0006	0.3683	0.0048	0.0536	0.0002	314 ± 4	318 ± 4	353 ± 8
SL-3-35-2	0.0909	218,625	13,000	0.0499	0.0007	0.3734	0.0055	0.0543	0.0002	314 ± 5	322 ± 4	381 ± 10
SL-3-36-1	0.0991	234,375	58,000	0.0496	0.0006	0.3637	0.0047	0.0530	0.0002	312 ± 4	314 ± 4	328 ± 9
SL-3-36-2	0.0790	188,938	29,000	0.0491	0.0006	0.3582	0.0048	0.0528	0.0002	308 ± 4	310 ± 4	318 ± 9
SL-3-37	0.0309	67,188	7000	0.0400	0.0006	0.3037	0.0049	0.0544	0.0003	252 ± 4	269 ± 4	387 ± 12

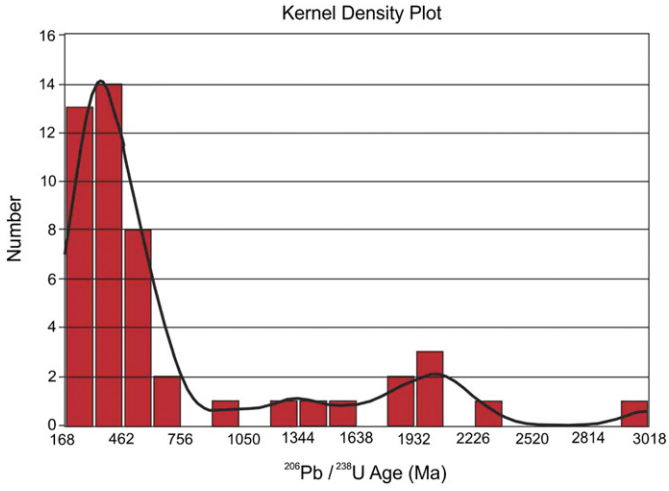

Fig. 13. Distributions of the different ages from SL-3 (granite sample).

with the CP, is also a part of this oceanic domain, and represents a back-arc of Middle Jurassic age (Okay et al., 2014; Çimen, 2016). The Çangaldağ Pluton and the Devrekani Granitoid (Nzegge, 2008) are the next units located to the north of the CPSC. Both have intruded the Eurasian continent margin comprising the Devrekani and Küre units, and represent the continental arc formed by the same subduction system that produced the CPSC. The results from this study confirm the continental arc character of the Çangaldağ Pluton based on its petrogenetic characteristics and zircon ages, and suggest that this continental crust is the source of the arc magma.

Based on the local and regional evidences in the Eastern Pontides and Caucasus, the CP may have been formed by northward subduction along the northernmost trench of the Mesozoic Intra-Pontide oceanic crust during the Middle Jurassic (Fig. 15). In this model, we suggest a multiple subduction system, similar to that in SE Asia (e.g. Hall, 2011). The main reasons for this interpretation are as follows.

a- Based on radiolarite–basalt associations in different slices of the mélange complexes of the CPSC, the formation ages of the IPO oceanic

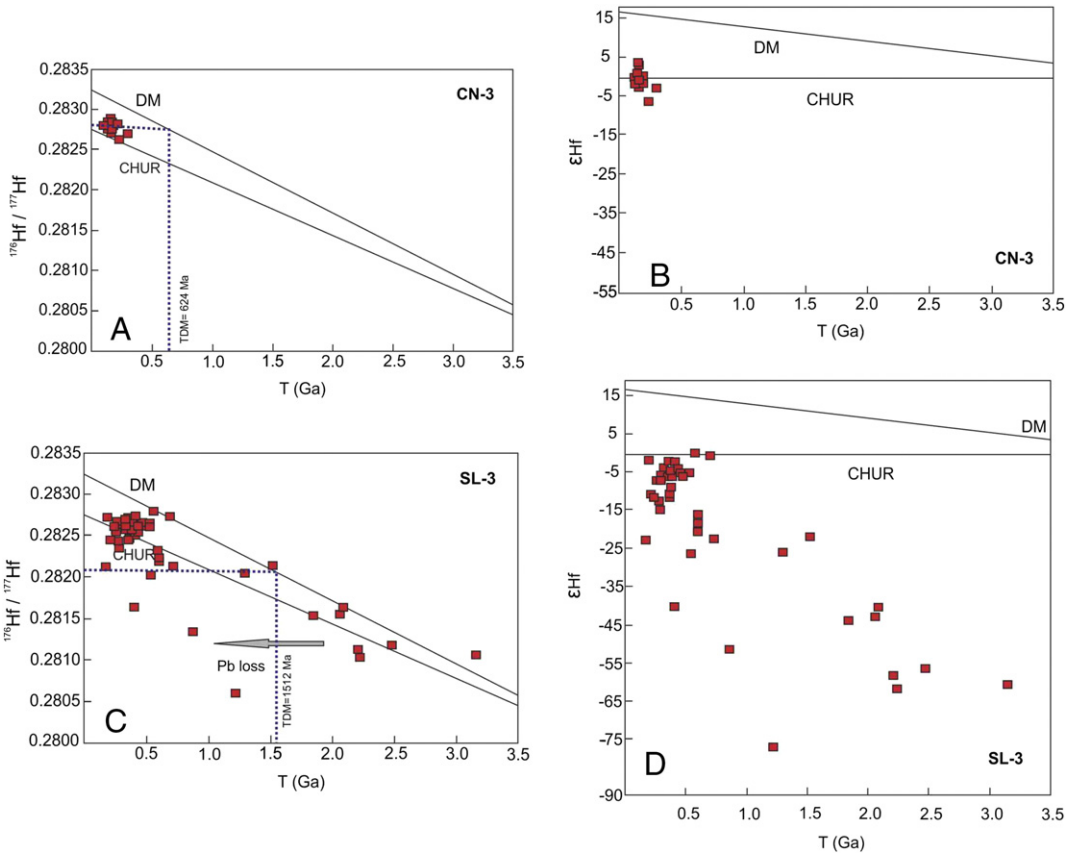

Fig. 14. $^{176}Hf/^{177}Hf$ (A, C) and εHf (B, D) vs Time diagrams for CN-3 and SL-3 samples. The εHf and TDM age values were calculated using the following formulas; $\varepsilon Hf = [(^{176}Hf/^{177}Hf)_{SMP} / (^{176}Hf/^{177}Hf)_{CHUR} - 1] \times 10^4$; $Hf\,T_{DM} = 1/\lambda \times Ln \times [(^{176}Hf/^{177}Hf)_{SMP} - (^{176}Hf/^{176}Hf)_{DM} / (^{176}Lu/^{177}Hf)_{SMP} - (^{176}Lu/^{176}Hf)_{DM} + 1]$. Here, $^{176}Lu/^{177}Hf_{DM} = 0.0384$ (Griffin et al., 2002). $^{176}Hf/^{177}Hf_{DM} = 0.28325$ (Griffin et al., 2002). $^{176}Hf/^{177}Hf_{CHUR} = 0.282785$ (Bouvier et al., 2008). For age correction: $^{176}Hf/^{177}Hf_{in} = ^{176}Hf/^{177}Hf_{meas} - ^{176}Lu/^{177}Hf\,(e^{\lambda t} - 1)$. $\lambda = 1.867 \times 10^{-11}\ yr^{-1}$ (Scherer et al., 2001).

crust range from Late Triassic to Early Cretaceous (Catanzariti et al., 2013; Göncüoğlu et al., 2012, 2014; Tekin et al., 2012).

b- In different tectonic units of the CPSC, the available Ar/Ar mineral ages indicate three distinct age-groups; 160–150 Ma (early Late Jurassic), 120–110 Ma (late Early Cretaceous and 90–100 Ma (early Late Cretaceous), suggesting three distinct episodes of metamorphism (Aygül et al., 2016; Frassi et al., 2017; Marroni et al., 2014; Okay et al., 2014).

c- Contemporaneous crust formation at different tectono-magmatic settings, or formation of the same-type oceanic crust at different times (Göncüoğlu et al., 2008, 2012, 2014).

These evidences suggest that there should be more than one subduction regime either along-strike of a single trench or at different segments within the closing IPO during the Middle Jurassic–Late Cretaceous interval. In the latter case, the segments may have been separated by transform faults, similar to the subduction systems elsewhere in the Alpine system (e.g. Dewey and Casey, 2011). Accordingly, in Fig. 15, Prism 2 may represent the accreted arc and back-arc-type oceanic crust (Domuzdağ, Saka, and Daday units of Sayit et al., 2016), which includes the oldest HP/LT assemblages during the early Late Jurassic. Prism 1 represents accreted non-metamorphic material of the Middle Jurassic arc–back-arc-type oceanic lithosphere (the Aylı Dağ ophiolite, Göncüoğlu et al., 2012), and the early Late Cretaceous Arkot Dağ mélange (e.g. Göncüoğlu et al., 2014). The latter unit is also non-metamorphic but comprises slide-blocks of the early Late Jurassic HP/LT rocks. The arc-basin assemblages (with fore-arc, island-arc and back-arc complexes) that now represent the Çangaldağ Metamorphic Complex were formed during the Middle Jurassic in a supra-subduction setting (Çimen, 2016). The LT/LP metamorphism of this unit occurred in the late Early Cretaceous (e.g. Aygül et al., 2016), and hence its subduction and accretion should have preceded formation of

Table 4
Hf isotope data for zircons in the dacite porphyry sample.

Grain #	$^{176}Hf/^{177}Hf$	SE	T_{DM} (Ma)	εHf	$^{176}Lu/^{177}Hf$	$^{173}Yb/^{177}Hf$	$^{178}Hf/^{177}Hf$	SE	Total Hf Int (V)
CN-3-1	0.28277	0.00003	656	−0.4	0.00127	0.04792	1.46727	0.00005	2.00918
CN-3-2	0.28287	0.00003	556	3.1	0.00363	0.16577	1.46731	0.00004	2.06990
CN-3-3-1	0.28277	0.00002	669	−0.5	0.00181	0.07439	1.46727	0.00005	2.06109
CN-3-3-2	0.28277	0.00002	677	−0.6	0.00194	0.08069	1.46723	0.00004	1.92049
CN-3-4	0.28280	0.00002	624	0.6	0.00167	0.07284	1.46730	0.00004	2.35007
CN-3-5	0.28279	0.00003	673	0.1	0.00332	0.14576	1.46737	0.00005	1.96434
CN-3-6	0.28277	0.00002	693	−0.5	0.00312	0.16027	1.46719	0.00003	2.80073
CN-3-8	0.28276	0.00003	674	−0.7	0.00153	0.06839	1.46724	0.00004	2.15573
CN-3-9	0.28271	0.00002	749	−2.5	0.00180	0.07878	1.46719	0.00004	2.24974
CN-3-11	0.28272	0.00003	732	−2.3	0.00147	0.06700	1.46737	0.00004	2.60776

Table 5
Hf isotope data for zircons in the granite sample.

Grain #	$^{176}Hf/^{177}Hf$	SE	T_{DM} (Ma)	εHf	$^{176}Lu/^{177}Hf$	$^{173}Yb/^{177}Hf$	$^{178}Hf/^{177}Hf$	SE	Total Hf Int (V)
SL-3-1	0.28163	0.00002	2170	−41.0	0.00066	0.02672	1.46739	0.00003	2.93
SL-3-2	0.28204	0.00002	1645	−26.5	0.00095	0.03776	1.46720	0.00004	3.49
SL-3-3	0.28264	0.00002	855	−5.1	0.00194	0.07869	1.46736	0.00003	2.48
SL-3-4	0.28059	0.00002	3464	−77.7	0.00010	0.00448	1.46727	0.00003	3.26
SL-3-5	0.28221	0.00002	1427	−20.3	0.00140	0.05559	1.46729	0.00003	3.29
SL-3-6	0.28264	0.00002	843	−5.1	0.00146	0.05635	1.46725	0.00003	2.77
SL-3-7	0.28260	0.00002	875	−6.4	0.00066	0.02436	1.46739	0.00003	2.82
SL-3-8	0.28214	0.00002	1478	−22.7	0.00038	0.01144	1.46725	0.00003	3.14
SL-3-9	0.28164	0.00002	2179	−40.4	0.00116	0.04874	1.46734	0.00004	2.33
SL-3-10	0.28263	0.00002	836	−5.4	0.00060	0.02224	1.46733	0.00003	2.72
SL-3-11	0.28274	0.00002	688	−1.5	0.00075	0.02570	1.46737	0.00004	2.50
SL-3-12	0.28232	0.00002	1264	−16.6	0.00079	0.03214	1.46728	0.00003	2.33
SL-3-13	0.28279	0.00002	639	0.0	0.00119	0.04886	1.46734	0.00003	2.52
SL-3-14	0.28215	0.00002	1484	−22.6	0.00059	0.02443	1.46723	0.00003	2.54
SL-3-15	0.28238	0.00002	1176	−14.5	0.00053	0.02082	1.46724	0.00004	2.25
SL-3-16	0.28118	0.00002	2807	−56.7	0.00147	0.06248	1.46727	0.00004	2.85
SL-3-17	0.28246	0.00002	1077	−11.4	0.00107	0.03901	1.46727	0.00003	2.67
SL-3-18	0.28271	0.00002	762	−2.8	0.00188	0.07533	1.46733	0.00004	2.37
SL-3-19	0.28266	0.00002	808	−4.5	0.00094	0.03397	1.46715	0.00004	2.47
SL-3-20	0.28213	0.00002	1512	−23.1	0.00085	0.02862	1.46730	0.00003	2.75
SL-3-21	0.28271	0.00002	733	−2.5	0.00099	0.02856	1.46726	0.00004	2.04
SL-3-22	0.28133	0.00003	2546	−51.4	0.00051	0.02843	1.46734	0.00003	2.72
SL-3-23	0.28155	0.00002	2277	−43.5	0.00085	0.05487	1.46723	0.00004	2.65
SL-3-24	0.28247	0.00002	1080	−11.2	0.00144	0.01255	1.46717	0.00004	2.22
SL-3-25	0.28205	0.00003	1604	−26.2	0.00029	0.02583	1.46735	0.00004	2.31
SL-3-26	0.28113	0.00002	2816	−58.7	0.00057	0.03980	1.46725	0.00004	2.43
SL-3-27	0.28157	0.00002	2268	−43.1	0.00099	0.06208	1.46724	0.00003	2.54
SL-3-28	0.28107	0.00003	2969	−60.6	0.00165	0.01624	1.46735	0.00004	2.23
SL-3-29	0.28226	0.00002	1324	−18.5	0.00040	0.03244	1.46730	0.00004	2.21
SL-3-30	0.28260	0.00002	882	−6.5	0.00082	0.02833	1.46735	0.00004	2.34
SL-3-31	0.28253	0.00002	975	−9.0	0.00079	0.02868	1.46721	0.00004	2.24
SL-3-32	0.28105	0.00002	2940	−61.2	0.00099	0.04373	1.46740	0.00003	2.49
SL-3-33-1	0.28262	0.00003	856	−5.8	0.00093	0.03664	1.46720	0.00004	2.12
SL-3-33-2	0.28258	0.00002	908	−7.3	0.00063	0.02471	1.46729	0.00004	2.85
SL-3-34	0.28274	0.00003	709	−1.7	0.00130	0.05279	1.46731	0.00005	1.69
SL-3-35	0.28265	0.00002	817	−4.8	0.00086	0.03401	1.46727	0.00004	2.15
SL-3-36	0.28263	0.00002	849	−5.5	0.00097	0.04070	1.46725	0.00004	2.30
SL-3-37	0.28243	0.00002	1131	−12.7	0.00132	0.05971	1.46721	0.00004	1.87

the CP. It was most probably the northern edge of the same subducting slab that generated the CP marginal arc within the northerly located continent margin (Devrekani Metamorphics and the Küre Complex). This conclusion is supported by the fact that CMC and CP are contemporaneous, as shown by the zircon ages reported here and in Çimen (2016). The final closure of this ocean presumably did not occur earlier than Turonian, the youngest age of the radiolarian cherts within the Arkot Dağ mélange (e.g. Tekin et al., 2012; Göncüoğlu et al., 2014; Göncüoglu et al., 2015).

The proposed geodynamic model (Fig. 15) is compared with those from Okay et al. (2015) and Aygül et al. (2016), where both suggest that these oceanic and continental assemblages formed by stepwise

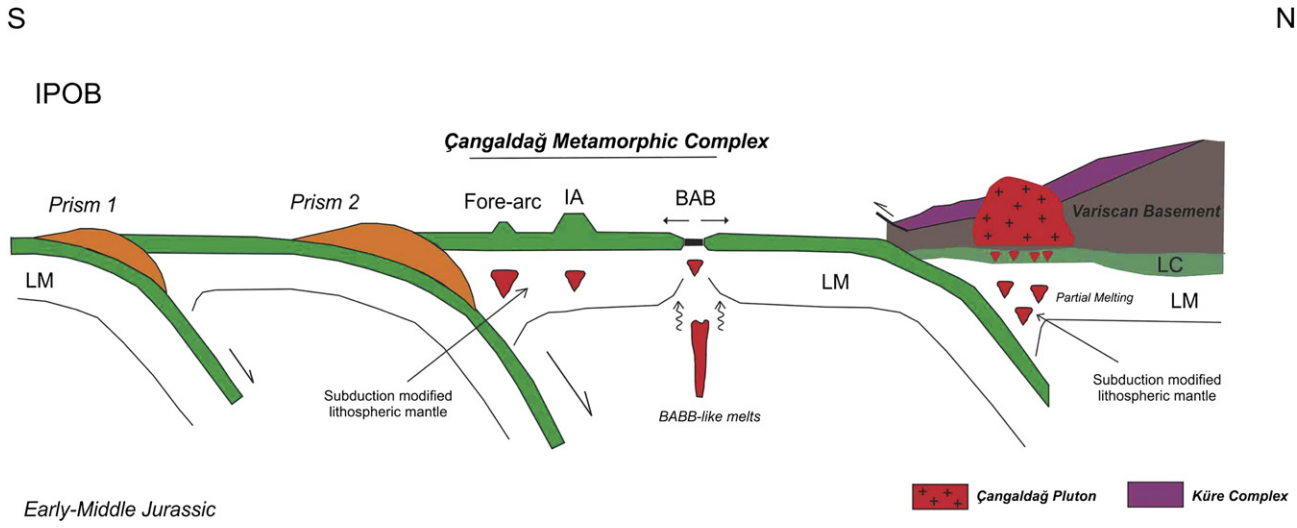

Fig. 15. Proposed geodynamic model for the Çangaldağ Pluton (Prism 1: Aylı Dağ Ophiolite and Arkot Dağ Melange; Prism 2: Domuzdağ, Daday and Saka Units; Variscan Basement: Devrekani Units, Geme Complex, Sivrikaya and Deliktaş Granitoids; LM: Lithospheric Mantle; IA: Island Arcs; BABB: Back-arc Basin Basalts; LC: Lower Crust).

accretion of the subduction–accretion complexes to the southern margin of the Rhodope-Pontide fragment. Our proposed hypothesis is in accordance with their stepwise accretion-model. However, we propose that the members of the CPSC, which display characteristics of fore arc–arc–back arc geotectonic settings (e.g. CMC, Domuz Dağ Unit, Aylı Dağ Unit and Daday Unit), indicate that there could be more than one intra-oceanic subduction system (Prisms 1 and 2; Fig. 15) within the closing IPO. Conversely, the continental arc magmatism, which is represented by several plutons (e.g. Çangaldağ and Karaman Plutons, Devrekani and Asarcık Diorites) may have formed above another subducting slab within the Variscan basement units such as the Devrekani Metamorphics and Geme Complex.

7. Conclusions

The CP, located in the northeast of the CMC, is composed predominantly of gabbroic diorites, dacite porphyries, and granites. Geologically, this large igneous body intrudes the Variscan Devrekani Metamorphics, the Triassic Küre Complex, and is overlain by Upper Jurassic İnalti Limestone. These field relations indicate an Early-Middle Jurassic age and are corroborated by the Middle Jurassic radiometric ages between 161 and 169 Ma reported here.

The rock units associated with the CP have similar geochemical characteristics consistent with volcanic arc granites. On the basis of calculated Hf T_{DM} model ages, these crustal rocks may be Neoproterozoic/Mesoproterozoic in age, which is common in Gondwana-derived terranes. The U–Pb ages and Hf isotope compositions reported here for zircons from the granite sample indicate detrital input from sedimentary sources; in contrast, the relatively consistent radiometric ages and Hf isotope data for zircons from the dacite porphyry is more consistent with derivation from a juvenile source.

In brief, evaluation of the petrogenetic features and ages of the variably metamorphosed oceanic-derived volcanics within the Central Pontide Structural Complex indicates that the Intra-Pontide Ocean was consumed by stepwise intra-oceanic subductions giving way to a huge subduction–accretion prism to the north of the Cimmerian Sakarya Composite Terrane. The CMC forms a back arc basin system above the subducting Intra-Pontide oceanic crust close to a Sakarya-type continental crust, whereas the CP represents the marginal (continental) arc above another subducting slab beneath the Küre and Devrekani units.

Acknowledgments

This research was supported by “Higher Educational Council of Turkey, OYP-PhD grant”, “The Scientific and Technological Research Council of Turkey, 114Y422 project” and “University of Notre Dame”. Also, many thanks to Çağrı Alperen İnan, Alican Aktağ and Uğur Balcı for their field assistance and Drs. Ian Steele, Elizabeth C. Koeman, and Zehra Deveci for their laboratory assistance. The authors gratefully acknowledge the comments of two anonymous referees and Dr. G.Nelson Eby, which has resulted in an improved manuscript.

References

Akbayram, K., Okay, A.I., Satır, M., 2013. Early Cretaceous closure of the Intra-Pontide Ocean in western Pontides (northwestern Turkey). Journal of Geodynamics 65, 38–55.

Akbayram, K., Şengör, A.M.C., Özcan, E., 2016. The evolution of the Intra-Pontide suture: Implications of the discovery of late Cretaceous–early Tertiary mélanges. GSA Special Papers 525.

Aydın, M., Demir, O., Özçelik, Y., Terzioğlu, N., Satır, M., 1995. A geological revision of İnebolu, Devrekani, Ağlı and Küre areas: new observations in Paleo-Tethys–Neo-Tethys sedimentary successions. In: Erler, A., Ercan, T., Bingöl, E., Örçen, S. (Eds.), Geology of the Black Sea Region. MTA/JMO, pp. 33–38.

Aygül, M., Okay, A.I., Oberhänsli, R., Sudo, M., 2016. Pre-collisional accretionary growth of the southern Laurasian active margin, Central Pontides, Turkey. Tectonophysics 671, 218–234.

Batumike, J.M., O'Reilly, S.Y., Griffin, W.L., Belousova, E.A., 2007. U–Pb and Hf-isotope analyses of zircon from the Kundelungu Kimberlites, D.R. Congo: implications for crustal evolution. Precambrian Research 156, 195–225.

Bouvier, A., Vervoot, J.D., Patchett, P.J., 2008. The Lu–Hf and Sm–Nd isotopic composition of CHUR: constraints from unequilibrated chondrites and implications for the bulk composition of terrestrial planets. Earth and Planetary Science Letters 273, 48–57.

Bozkurt, E., Winchester, J.A., Satır, M., 2013. The Çele mafic complex: evidence for Triassic collision between the Sakarya and İstanbul Zones, NW Turkey. Tectonophysics 595-596, 198–214.

Boztuğ, D., Yılmaz, O., 1995. Daday-Devrekani masifi metamorfizması ve jeolojik evrimi, Kastamonu bölgesi, Batı Pontidler, Türkiye. TJ. Bülteni 38, 33–52 (in Turkish).

Boztuğ, D., Debon, F., Le Fort, P., Yılmaz, O., 1995. High compositional diversity of the Middle Jurassic Kastamonu Plutonic Belt, northern Anatolia, Turkey. Turkish Journal of Earth Sciences 4, 67–86.

Catanzariti, R., Ellero, A., Göncüoğlu, M.C., Marroni, M., Ottria, G., Pandolfi, L., 2013. The Taraklı Flysch in the Boyali area (Sakarya Terrane, northern Turkey): implications for the tectonic history of the Intra-Pontide suture zone. Comptes Rendus Geoscience 345, 454–461.

Chen, W., Simonetti, A., 2014. Evidence for the multi-stage petrogenetic history of the Oka carbonatite complex (Quebec, Canada) as recorded by perovskite and apatite. Minerals 4, 437–476.

Chen, F., Siebel, W., Satır, M., Terzioğlu, N., Saka, K., 2002. Geochronology of the Karadere basement (NW Turkey) and implications for the geological evolution of the İstanbul Zone. International Journal of Earth Sciences 91, 469–481.

Çimen, 2016. The Petrology and Geochronology of the Igneous Rocks From the Çangaldağ Metamorphic Complex and the Çangaldağ Pluton (Central Pontides-Turkey), Central Pontides. Middle East Technical University (PhD Thesis, 254 pp.).

Çimen, O., Göncüoğlu, M.C., Sayit, K., 2016. Geochemistry of the meta-volcanic rocks from the Çangaldağ Complex in Central Pontides: implications for the Middle Jurassic arc–back-arc system in the Neotethyan Intra-Pontide Ocean. Turkish Journal of Earth Sciences 25, 491–512.

Condie, K.C., Kroner, A., 2013. The building blocks of continental crust: evidence for a major change in the tectonic setting of continental growth at the end of the Archean. Gondwana Research 23, 394–402.

Dean, W.T., Martin, F., Monod, O., Demir, O., Rickards, A.B., Boltynck, P., Bozdoğan, N., 1997. Lower Paleozoic stratigraphy, Karadere-Zirze area, Central Pontides, northern Turkey. Geological Magazine 137, 555–582.

Dewey, J.F., Casey, J.F., 2011. The origin of obducted large-slab ophiolite complexes. Arc–Continent Collision. Springer, Berlin Heidelberg, pp. 431–444.

Dokuz, A., Karsli, O., Chen, B., Uysal, İ., 2010. Sources and petrogenesis of Jurassic granitoids in the Yusufeli area, Northeastern Turkey: implications for pre- and post-collisional lithospheric thinning of the eastern Pontides. Tectonophysics 480, 259–279.

Dokuz, A., Aydınçakır, E., Kandemir, R., Karslı, O., Siebel, W., Derman, A.M., Turan, M., 2017. Late Jurassic magmatism and stratigraphy in the Eastern Sakarya Zone, Turkey: evidence for the slab breakoff of Paleotethyan oceanic lithosphere. The Journal of Geology 125, 1–31.

Elmas, A., Yiğitbaş, E., 2001. Ophiolite emplacement by strike-slip tectonics between the Pontide Zone and the Sakarya Zone in northwestern Anatolia, Turkey. International Journal of Earth Sciences 90, 257–269.

Floyd, P.A., Winchester, J.A., 1978. Identification and discrimination of altered and metamorphosed volcanic rocks using immobile elements. Chemical Geology 21, 291–306.

Frassi, C., Göncüoğlu, M.C., Marroni, M., Pandolfi, L., Ruffini, L., Ellero, A., Ottria, G., Sayit, K., 2016. The Intra-Pontide suture zone in the Tosya-Kastamonu area, Northern Turkey. Journal of Maps 12, 211–219.

Frassi, C., Marroni, M., Pandolfi, L., Göncüoğlu, M.C., Ellero, A., Ottria, G., Sayit, K., Mcdonald, C.S., Balestrieri, M.L., Malasoma, A., 2017. Burial and exhumation history of the Daday Unit (Central Pontides, Turkey): implications for the closure of the Intra-Pontide oceanic basin. Geological Magazine http://dx.doi.org/10.1017/S0016756817000176.

Genc, S.C., Tüysüz, O., 2010. Tectonic setting of the Jurassic bimodal magmatism in the Sakarya Zone (Central and Western Pontides), Northern Turkey: a geochemical and isotopic approach. Lithos 118, 95–111.

Göncüoğlu, M.C., 2010. Introduction to the Geology of Turkey: Geodynamic Evolution of the Pre-Alpine and Alpine Terranes. MTA, pp. 1–69.

Göncüoğlu, M.C., Turhan, N., Sentür, k, K., Özcan, A., Uysal, S., 2000. A geotraverse across NW Turkey: tectonic units of the Central Sakarya region and their tectonic evolution. In: Bozkurt, E., Winchester, J.A., Piper, J.D. (Eds.), Tectonics and Magmatism in Turkey and the Surrounding Area. Geological Society of London, Special Publications vol. 173, pp. 139–162.

Göncüoğlu, M.C., Gürsu, S., Tekin, U.K., Köksal, S., 2008. New data on the evolution of the Neotethyan Oceanic Branches in Turkey: Late Jurassic ridge spreading in the Intra-Pontide Branch. Ofioliti 33, 153–164.

Göncüoğlu, M.C., Marroni, M., Sayit, K., Tekin, U.K., Ottria, G., Pandolfi, L., Ellero, A., 2012. The Aylı Dağ ophiolite sequence (Central-Northern Turkey): a fragment of Middle Jurassic Oceanic Lithosphere within the Intra-Pontide suture zone. Ofioliti 37, 77–92.

Göncüoğlu, M.C., Marroni, M., Pandolfi, L., Ellero, A., Ottria, G., Catanzariti, R., Tekin, U.K., Sayit, K., 2014. The Arkot Dağ Melange in Araç area, central Turkey: evidence of its origin within the geodynamic evolution of the intra-Pontide suture zone. Journal of Asian Earth Science 85, 117–139.

Göncüoğlu, M.C., Tekin, U.K., Sayit, K., Bedi, Y., Uzuncimen, S., 2015. Opening, evolution and closure of the Neotethyan oceanic branches in Anatolia as inferred by radiolarian research. Radiolaria 35, 88–90.

Gorton, M.P., Schandl, E.S., 2000. From continents to island arcs: a geochemical index of tectonic setting for arc-related and within-plate felsic to intermediate volcanic rocks. The Canadian Mineralogist 38, 1065–1073.

Griffin, W.L., Wang, X., Jackson, S.E., Pearson, N.J., O'Reilly, S.Y., Xu, X., Zhou, X., 2002. Zircon chemistry and magma mixing, SE China: in situ analysis of Hf isotopes, Tonglu and Pingtan igneous complexes. Lithos 61, 237–269.

Gücer, M.A., Arslan, M., Sherlock, S., Heaman, L.M., 2016. Permo-Carboniferous granitoids with Jurassic high temperature metamorphism in Central Pontides, Northern Turkey. Mineralogy and Petrology 110, 943–964.

Günay, K., Dönmez, C., Uysal, İ., Yıldırım, N., Şahin, M.B., Yıldırım, E., Tablacı, A., Kang, J., Lee, I., 2016. Chrome spinel geochemistry of ultramafic rocks from the Elekdağ metaophiolite (Northern Turkey): implications for greenschist to mid-amphibolite facies metamorphism. Neues Jahrbuch für Mineralogie (Abhandlungen) 193, 1–16.

Hall, R., 2011. Australia–SE Asia collision: plate tectonics and crustal flow. Geological Society, London, Special Publications 355, 75–109.

Horn, I., Rudnick, R.L., McDonough, W.F., 2000. Precise elemental and isotope ratio determination by simultaneous solution nebulization and laser ablation-ICP-MS: application to U–Pb geochronology. Chemical Geology 164, 281–301.

Jackson, S.E., Pearson, N.J., Griffin, W.L., Belousova, E.A., 2004. The application of laser ablation-inductively coupled plasma-mass spectrometry to in situ U–Pb zircon geochronology. Chemical Geology 211, 47–69.

Janoušek, V., Farrow, C.M., Erban, V., 2006. Interpretation of whole-rock geochemical data in igneous geochemistry: introducing Geochemical Data Toolkit (GCDkit). Journal of Petrology 47, 1255–1259.

Karslı, O., Dokuz, A., Kandemir, R., 2017. Zircon Lu–Hf systematics and U–Pb geochronology, whole-rock Sr–Nd isotopes and geochemistry of the early Jurassic Gokcedere pluton, Sakarya Zone-NE Turkey: a magmatic response to roll-back of the Paleo-Tethyan oceanic lithosphere. Contributions to Mineralogy and Petrology 172, 1–27.

Kaya, M.Y., Altıner, D., 2014. Terebella lapilloides Münster, 1833 from the Upper Jurassic-Lower Cretaceous İnalti carbonates, northern Turkey: its taxonomic position and paleoenvironmentalpaleoecological significance. Turkish Journal of Earth Sciences 23, 166–183.

Ketin, İ., Gümüş, A., 1963. Sinop – Ayancık güneyinde üçüncü bölgeye dahil sahaların jeolojisi hakkında rapor (2. Kısım: Jura ve Kretase formasyonlarının etüdü). TPAO Report Number. 288.

Konya, S., Pehlivanoğlu, H., Teşrekli, M., 1988. Kastamonu, Taşköprü, Devrekani yöresi jeokimya raporu. MTA (in Turkish). Report Number: 8341.

Kozur, H., Aydın, M., Demir, O., Yakar, H., Göncüoğlu, M.C., Kuru, F., 2000. New stratigraphic results from the Paleozoic and Early Mesozoic of the Middle Pontides (Northern Turkey). Geologia Croatica 53, 209–268.

Kröner, A., Hoffmann, J.E., Xie, H., Münker, C., Hegner, E., Wan, Y., Hofmann, A., Liu, D., Yang, J., 2014. Generation of early Archaean grey gneisses through melting of older crust in the eastern Kaapvaal craton, southern Africa. Precambrian Research 255, 823–846.

Ludwig, K.R., 2008. Manual for Isoplot 3.7: Berkeley Geochronology Center, Special Publication 4. p. 77.

Marroni, M., Frassi, C., Göncüoğlu, M.C., Dl Vincenzo, G., Pandolfi, L., Rebay, G., Ellero, A., Ottaria, G., 2014. Late Jurassic amphibolite-facies metamorphism in the Intra-Pontide Suture Zone (Turkey): an eastward extension of the Vardar Ocean from the Balkans into Anatolia? Journal of Geological Society 171, 605–608.

McCann, T., Chalot-Prat, F., Saintot, A., 2010. The Early Mesozoic evolution of the Western Greater Caucasus (Russia): Triassic–Jurassic sedimentary and magmatic history. Geological Society of London, Special Publication 340, 181–238.

Meijers, M.J.M., Vrouwe, B., van Hinsbergen, D.J.J., 2010. Jurassic arc volcanism on Crimea (Ukraine): implications for the paleo-subduction zone configuration of the Black Sea region. Lithos 119, 412–426.

Miyashiro, A., 1974. Volcanic arc series in island arcs and active continental margins. American Journal Science 274, 321–335.

Nzegge, O., 2008. Petrogenesis and Geochronology of the Deliktaş, Sivrikaya and Devrekani Granitoids and Basement, Kastamonu Belt-Central Pontides (NW Turkey): Evidence for Late Paleozoic–Mesozoic Plutonism, and Geodynamic Interpretation. (PhD Thesis). p. 177.

Okay, A.I., Göncüoğlu, M.C., 2004. Karakaya Complex: a review of data and concepts. Turkish Journal of Earth Sciences 13, 77–95.

Okay, A.I., Nikishin, M.A., 2015. Tectonic evolution of the southern margin of Laurasia in the Black Sea region. International Geology Review 1–26.

Okay, A.I., Tüysüz, O., 1999. Tethyan sutures of northern Turkey. In: Durand, B., Jolivet, L., Horvath, F., Seranne, M. (Eds.), The Mediterranean Basins: Tertiary Extension Within the Alpine Orogen. Geological Society of London, Special Publication 156, pp. 475–515.

Okay, A.I., Tüysüz, O., Satır, M., Özkan-Altıner, S., Altıner, D., Sherlock, S., Eren, R.H., 2006. Cretaceous and Triassic subduction–accretion, high-pressure–low-temperature metamorphism, and continental growth in the Central Pontides, Turkey. GSA Bulletin 118, 1247–1269.

Okay, A.I., Bozkurt, E., Satır, M., Yiğitbaş, E., Crowley, Q.G., Shang, C.K., 2008. Defining the southern margin of Avalonia in the Pontides: geochronological data from the Late Proterozoic and Ordovician granitoids from NW Turkey. Tectonophysics 461, 252–264.

Okay, A.I., Gürsel, S., Sherlock, S., Altıner, D., Tüysüz, O., Kylander-Clark, A.R.C., Aygül, M., 2013. Early Creataceous sedimentation and orogeny on the active margin of Eurasia: Southern Central Pontides, Turkey. Tectonics 32, 1247–1271.

Okay, A.I., Gürsel, S., Tüysüz, O., Sherlock, S., Keskin, M., Kylander-Clark, A.R.C., 2014. Low-pressure–high-temperature metamorphism during extension in a Jurassic magmatic arc, Central Pontides, Turkey. Journal of Metamorphic Geology 32, 49–69.

Okay, A.I., Altıner, D., Kılıç, A., 2015. Triassic limestone, turbidites and serpentinite—the Cimmeride orogeny in the central Pontides. Geological Magazine 152, 460–479.

Özgül, N., 2012. Stratigraphy and some structural features of the İstanbul Paleozoic. Turkish Journal of Earth Sciences 21, 817–866.

Paton, C., Woodhead, J.D., Hellstrom, J.C., Hergt, J.M., Greig, A., Maas, R., 2010. Improved laser ablation U–Pb zircon geochronology through robust downhole fractionation correction. Geochemistry Geophysics Geosystems (G^3) 11, 1–36.

Pearce, J.A., Cann, J.R., 1973. Tectonic setting of basic volcanic rocks determined using trace element analyses. Earth and Planetary Science Letters 19, 290–300.

Pearce, J.A., Peate, D.W., 1995. Tectonic implications of the composition of volcanic arc magmas. Annual Review of Earth and Planetary Sciences 23, 251–286.

Pearce, J.A., Harris, N.W., Tindle, A.G., 1984. Trace element discrimination diagrams for the tectonic interpretation of granitic rocks. Journal of Petrology 25, 956–983.

Pearce, J.A., Stern, R.J., Bloomer, S.H., Fryer, P., 2005. Geochemical mapping of the Mariana arc-basin system: implications for the nature and distribution of subduction components. Geochemical Geophysical Geosystems 6, 1–27.

Pearson, N.J., Griffin, W.L., O'Reilly, S.Y., 2008. Mass fractionation correction in laser ablation multiple-collector ICP-MS: precise and accurate *in situ* isotope ratio measurement. In: Sylvester, P. (Ed.), Laser Ablation-ICP-MS in the Earth Sciences. Mineralogical Association of Canada Short Course Series vol. 40, pp. 93–116.

Rapela, C.W., Verdecchia, S.O., Casquet, C., Pankhurst, R.J., Baldo, E.G., Galindo, C., Murra, J.A., Dalhquist, J.A., Fanning, C.M., 2016. Identifying Laurentian and SW Gondwana sources in the Neoproterozoic to Early Paleozoic metasedimentary rocks of the Sierras Pampeanas: paleogeographic and tectonic implications. Gondwana Research 32, 193–212.

Robertson, A.H.F., Ustaömer, T., 2004. Tectonic evolution of the Intra-Pontide suture zone in the Armutlu Peninsula, NW Turkey. Tectonophysics 381, 175–209.

Robertson, A., Parlak, O., Ustaömer, T., Taslı, K., İnan, N., Dumitrica, P., Karaoğlan, F., 2014. Subduction, ophiolite genesis and collision history of Tethys adjacent to the Eurasian continental margin: new evidence from the Eastern Pontides, Turkey. Geodinamica Acta 1–64.

Şahin, S.Y., Güngör, Y., Aysal, N., Öngen, S., 2009. Geochemistry and SHRIMP zircon U–Pb dating of granitoids within the Strandja and Istanbul Zones (NW Turkey). Abstracts, 62nd Geological Congress of Turkey, Ankara, pp. 598–599.

Sayit, K., Göncüoğlu, M.C., 2009. Geochemistry of mafic rocks of the Karakaya complex, Turkey: evidence for plume-involvement in the Palaeotethyan extensional regime during the Middle and Late Triassic. International Journal of Earth Sciences 98, 157–185.

Sayit, K., Marroni, M., Göncüoğlu, M.C., Pandolfi, L., Ellero, A., Ottria, G., Frassi, C., 2016. Geological setting and geochemical signatures of the mafic rocks from the Intra-Pontide Suture Zone: implications for the geodynamic reconstruction of the Mesozoic Neotethys. International Journal of Earth Sciences 105, 39–64.

Schandl, E.S., Gorton, M.P., 2002. Application of high field strength elements to discriminate tectonic settings in VMS environments. Economic Geology 97, 629–642.

Scherer, E.E., Münker, C., Mezger, K., 2001. Calibration of the Lu–Hf clock. Science 293, 683–687.

Schmidberger, S.S., Heaman, L.M., Simonetti, A., Creaser, R.A., Cookenboo, H.O., 2005. Formation of Paleoproterozoic eclogicitic mantle, slave province (Canada): insights from in-situ Hf and U–Pb isotope analyses of mantle zircons. Earth and Planetary Science Letters 240, 621–633.

Şen, C., 2007. Jurassic volcanism in the Eastern Pontides: is it rift related or subduction related? Turkish Journal of Earth Sciences 16, 523–539.

Şen, Ş., 2013. New evidences for the formation of and for petroleum exploration in the fold-thrust zones of the central Black Sea Basin of Turkey. American Association of Petroleum Geologists Bulletin 97, 465–485.

Şengör, A.M.C., Yılmaz, Y., 1981. Tethyan evolution of Turkey: a plate tectonic approach. Tectonophysics 75, 181–241.

Simonetti, A., Neal, C.R., 2010. In-situ chemical U–Pb dating and Hf isotope investigation of megacrystic zircons, Malaita (Solomon Islands): evidence for multiple stage alkaline magmatic activity beneath the Ontong Java Plateau. Earth and Planetary Science Letters 295, 251–261.

Simonetti, A., Heaman, L.R., Hartlaub, R., Creaser, T., MacHattie, T.G., Böhm, C., 2005. U–Pb zircon dating by laser ablation-MC-ICP-MS using a new multiple ion counting Faraday collector array. Journal of Analytical Atomic Spectrometry 20, 677–686.

Slama, J., Kosler, J., Condon, D.J., Crowley, J.L., Gerdes, A., Hanchar, J.M., Horstwood, M.S.A., Morris, G.A., Nasdala, L., Norberg, N., Schaltegger, U., Schoene, N., Tubrett, M.N., Whitehouse, M.J., 2008. Plesovice zircon — a new natural reference material for U–Pb and Hf isotopic microanalysis. Chemical Geology 249 (1–2), 1–35.

Stampfli, G.M., Borel, G.D., 2002. A plate tectonic model for the Palaeozoic and Mesozoic constrained by dynamic plate boundaries and restored synthetic oceanic isochrones. Earth and Planetary Science Letters 169, 17–33.

Sun, S.S., McDonough, W.F., 1989. Chemical and isotopic systematics of oceanic basalts: implications for mantle composition and processes. Geological Society, London, Special Publications 42, 313–345.

Tekin, U.K., Göncüoğlu, M.C., Pandolfi, L., Marroni, M., 2012. Middle Late Triassic radiolarian cherts from the Arkotdağ melange in northern Turkey: implications for the life span of the northern Neotethyan branch. Geodinamica Acta 25, 305–319.

Tera, F., Wasserburg, G.J., 1972. U–Th–Pb systematics in lunar highland samples from the Luna 20 and Apollo 16 missions. Earth and Planetary Science Letters 17, 36–51.

Topuz, G., Altherr, R., Satır, M., Schwarz, W.H., 2004. Low-grade metamorphic rocks from the Pulur complex, NE Turkey: implications for the pre-Liassic evolution of the Eastern Pontides. International Journal of Earth Sciences 93, 72–91.

Tüysüz, O., 1990. Tectonic evolution of a part of the Tethyside orogenic collage: the Kargı Massif, northern Turkey. Tectonics 9, 141–160.

Tüysüz, O., 1999. Geology of the Cretaceous sedimentary basins of the Western Pontides. Geological Journal 34, 75–93.

Uğuz, M.F., Sevin, M., 2007. Türkiye Jeoloji Haritaları, Kastamonu-E32 Paftası. Jeoloji Etütleri Dairesi 32 s (in Turkish).

Ustaömer, T., Robertson, A.H.F., 1999. Geochemical evidence used to test alternative plate tectonic models for pre-Upper Jurassic (Palaeotethyan) units in the Central Pontides, N Turkey. Geological Journal 34, 25–53.

Ustaömer, P.A., Mundil, R., Renne, P.R., 2005. U/Pb and Pb/Pb zircon ages for arc-related intrusions of the Bolu Massif (W Pontides, NW Turkey): evidence for Late Precambrian (Cadomian) age. Terra Nova 17, 215–223.

Wiedenbeck, M., Alle, P., Corfu, F., Griffin, W.L., Meier, M., Oberli, F., von Quadt, A., Roddick, J.C., Spiegel, W., 1995. Three natural zircon standards for U–Th–Pb, Lu–Hf, trace element and REE analyses. Geostandards Newsletter 19, 1–23.

Winchester, J.A., Floyd, P.A., 1977. Geochemical discrimination of different magma series and their differentiation products using immobile elements. Chemical Geology 20, 325–343.

Woodhead, J.D., Hergt, J.M., 2005. Preliminary appraisal of seven natural zircon reference materials for in situ Hf isotope determination. Geostandards and Geoanalytical Research 29, 183–195.

Woodhead, J., Hergt, J., Shelley, M., Eggins, S., Kemp, R., 2004. Zircon Hf-isotope analysis with an excimer laser, depth profiling ablation of complex geometries, and concomitant age estimation. Chemical Geology 209, 121–135.

Yılmaz, O., 1983. Çangal metaofiyolitinin mineralojik-petrografik incelenmesi ve metamorfizma koşulları. Yerbilimleri 10, 45–58 (in Turkish).

Yılmaz, O., Bonhomme, M.G., 1991. K–Ar isotopic age evidence for a Lower to Middle Jurassic low-pressure and a Lower Cretaceous high-pressure metamorphic events in north-central Turkey. Terra Abstracts 3, 501.

Yılmaz, O., Boztuğ, D., 1986. Kastamonu granitoid belt of northern Turkey: first arc plutonism product related to the subduction of the Paleo-Tethys. Geology 14, 179–183.

Yılmaz, Y., Tüysüz, O., Yiğitbaş, E., Genç, C.Ş., Şengör, A.M.C., 1997. Geology and tectonic evolution of the Pontides. In: Robinson, A.G. (Ed.), Regional and Petroleum Geology of the Black Sea and Surrounding Region. American Association of Petroleum Geologists, Memoir vol. 68, pp. 183–226.